Advances in Water Resources 156 (2021) 104039

Contents lists available at ScienceDirect

Advances in Water Resources

journal homepage: www.elsevier.com/locate/advwatres

Discontinuous and continuous Galerkin methods for compressible single-phase and two-phase flow in fractured porous media

Tianran Ma [a,b], Keni Zhang [c], Weijun Shen [d,e,*], Chaobin Guo [f], Hao Xu [c]

[a] School of Mechanics and Civil Engineering, China University of Mining and Technology, Xuzhou, Jiangsu 221116, China
[b] State Key Laboratory Geomechanics and Deep Underground Engineering, China University of Mining and Technology, Xuzhou, Jiangsu 221116, China
[c] Lawrence Berkeley National Laboratory, Energy Geosciences Division, Berkeley, CA 94720, United States
[d] Key Laboratory for Mechanics in Fluid Solid Coupling Systems, Institute of Mechanics, Chinese Academy of Sciences, Beijing 100190, China
[e] School of Engineering Science, University of Chinese Academy of Sciences, Beijing 100049, China
[f] Chinese Academy of Geological Sciences, Beijing 100037, China

ARTICLE INFO

Keywords:
Fractured porous media
Discontinuous Galerkin
Compressible flow
Discrete fractured model

ABSTRACT

Accurate simulation of flow behaviors in fractured porous media is challenging. We present a discontinuous Galerkin (DG) approximation and continuous Galerkin (CG) approximation for compressible single- and two-phase flow in porous media with conducting (high permeable) and blocking (low permeable) fractures using a mixed-dimensional approach in which the fracture is described as a reduced-dimensional interface coupled with linear transmission conditions. The proposed DG/CG method was first verified with single-phase fractured flow benchmark cases and then applied to time-dependent single-phase flow cases. The simulated results demonstrate that the DG/CG method is capable of capturing the continuity as well as the jump in pressure between the two sides of the matrix-fracture interface. For the two-phase flow cases, we verify the DG/CG method with a reference case involving a complex fracture configuration. Subsequently, we analyze several cases to study two-phase flow through a single fracture and a discrete fracture network in two dimensions. Overall, the simulation results show that the developed DG/CG approach can reliably predict the flow behaviors for single- and two-phase flow in fractured porous media.

1. Introduction

Modeling of fluid flow in fractured porous media is of significance in a variety of applications, such as geothermal extraction (Lepillier et al., 2019; Salimzadeh and Nick, 2019), geological carbon storage (R March et al., 2018; Ren et al., 2017), gas and oil exploitation (Khoei et al., 2016; Jiang and Yang, 2018; Ma et al., 2020) and contaminant migration in reservoirs (Saiers and Barth, 2012). Fractures are capable of forming conductive paths or barriers as a result of different hydraulic properties between fractures and the rock matrix. The discontinuous material properties as well as spatial scales have a great influence on flow paths associated with the injection or production of fluids.

A series of conceptual models across multiple scales have been developed to describe single- and multiphase flow in fractured porous media. Generally, two main approaches, continuum models (R March et al., 2018; Warren and Root, 1963; Wu et al., 2004) and discrete fracture models (Gläser et al., 2019; Gläser et al., 2017; Hoteit and Firoozabadi, 2008; Jin and Zoback, 2017), have been proposed. The continuum models are categorized into single- and multicontinuum models. In single-continuum models, the equivalent permeability of the reservoir is calculated with an upscaling technique combined with the fracture information involving the surface roughness, aperture and orientation (Oda, 1985). In multicontinuum models, the classic dual-porosity double-permeability (DPDP) model has been widely used for the simulation of fluid flow in unconventional gas extraction (Yang et al., 2019) and CO_2 sequestration (R March et al., 2018). Although this type of approach is efficient with low computational cost, the calculation of the flux exchange between the matrix and fracture remains a challenge, especially with consideration of gravity and capillarity in two-phase flow (Hoteit and Firoozabadi, 2008; Zidane and Firoozabadi, 2017). The alternative approach uses the discrete fracture model, where the fractures are described individually by lower-dimensional fracture elements as the predominant conductive or impeditive impacts on the flow path. This method is suitable for the case where the fracture rupture

* Corresponding author.
E-mail address: wjshen763@imech.ac.cn (W. Shen).

https://doi.org/10.1016/j.advwatres.2021.104039
Received 8 May 2021; Received in revised form 8 August 2021; Accepted 8 September 2021
Available online 11 September 2021

is much smaller than the size of the matrix (Khoei et al., 2016; Ma et al., 2020; Gläser et al., 2019; Gläser et al., 2017; Jin and Zoback, 2017; Brenner et al., 2018; Kadeethum et al., 2020). A reduced-dimensional model for the flow along a fracture and suitable coupling conditions on the matrix fracture interface were derived for single-phase Darcy problems in porous media in the presence of impermeable and permeable fractures (Martin et al., 2005) and later extended to two phases with linear and nonlinear transmission conditions on the interface (Aghili et al., 2019).

Various numerical methods, including the control volume finite element, cell-centered finite volume, extended finite element method and embedded discrete fracture method, have been developed to model fluid flow in fractured porous media. Two types of finite volume approaches have been proposed: the control-volume finite element method and cell-centered finite volume (FV) approach. Monteagudo and Firoozabadi employed the control-volume finite volume (CVFV) approach for two-phase flow in fractured media assuming capillary pressure and flux continuity at the matrix–fracture interface (Monteagudo and Firoozabadi, 2004). Reichenberger et al. also used the CVFV method to model two-phase flow in 2D fractured media. They introduced discontinuous approximation functions for saturation to capture the saturation discontinuity at the matrix–fracture interface caused by the capillary pressure difference between the matrix and fracture (Reichenberger et al., 2006); Karimi-Fard et al. introduced a cell-centered FV method with a two-point flux approximation (TPFA) and extended it to the multipoint flux approximation (MPFA) for the simulation of two-phase flow in fractured media (Karimi-Fard et al., 2004). Glaser performed discrete fracture-matrix modeling involving highly conductive and low-permeability fractures with the MPFA-DFM approach (Gläser et al., 2019; Gläser et al., 2017). D'Angelo and Scotti implemented the extended finite element method for single-phase Darcy flow in fractured porous media with nonmatching grids (D'Angelo and Scotti, 2012). Fumagalli and Scotti extended the method to a two-phase case by considering an additional equation for saturation (Fumagalli and Scotti, 2013). Additionally, Khoei developed a coupled hydromechanical model to simulate two-phase fluid flow through deformable fractured porous media using the extended finite element method (Khoei et al., 2016). Li et al. proposed the embedded discrete fracture method for simulating hydrocarbon exploitation (Li and Lee, 2008). Later, this method was improved and extended to projection-based EDFM (pEDFM) for modeling two-phase flow with a wide range of permeabilities (Jiang and Younis, 2017; Ţene et al., 2017).

Discontinuous Galerkin (DG) methods have the following advantages: (1) local mass conservation; (2) flexible mesh discretization; and (3) h–p adaptivity. DG methods have recently received substantial attention and have been applied to incompressible two-phase flow in porous media (D'Angelo and Scotti, 2012; Cappanera and Rivière, 2019; Epshteyn and Rivière, 2007) and steady single-phase flow in fractured porous media (Antonietti et al., 2019). Klieber and Riviere (Klieber and Riviere, 2006) presented adaptivity techniques to sequentially solve the wetting phase pressure-saturation equation with DG methods. Based on the work of Klieber and Rivier (Klieber and Riviere, 2006), Jamei and Ghafouri (Jamei and Ghafouri, 2016) presented a novel sequential implicit DG method for two-phase incompressible flow in homogenous and heterogeneous media based on velocity conservative projection. Arbogast et al. (Arbogast et al., 2013) and Bastian (Bastian, 2014) used DG methods to discretize two-phase flow formation with continuous capillary pressure and discontinuous capillary pressure, respectively. Later, the DG method was extended to simulations of multi-component and multi-phase flow problems (Cappanera and Rivière, 2019; Riviere and Yang, 2017; Zidane and Firoozabadi, 2020; Ern and Mozolevski, 2012). For fluid flow in fractured porous media, Antonietti et al. (Antonietti et al., 2019; Antonietti et al., 2020) simulated single-phase flow through a fractured porous medium with polygonal and polyhedral grids based on the DG method. Zidane and Firoozabadi (Zidane and Firoozabadi, 2020) studied compositional two-phase flow in a domain with non-planar fractures by combining a mixed finite element method and a high-order DG method. In previous studies (Hoteit and Firoozabadi, 2008; Zidane and Firoozabadi, 2017), the DG method was used with a mixed finite element approach to simulate incompressible and compressible two-phase flow in fractured media.

In this paper, we present a DG/CG approach for time-dependent compressible single-phase and two-phase flow in porous media with conducting and blocking fractures. The fluid flow in the porous media and fractures is approximated with the discontinuous and continuous Galerkin finite element methods, respectively. This paper is organized as follows. In Section 2, we first introduce the governing equations and the corresponding weak forms of single-phase flow in fractured porous media. Subsequently, a steady flow case with a complex fracture network is carried out to verify the accuracy of the proposed model. Later, we perform several time-dependent cases with a single fracture embedded horizontally in porous media. In Section 3, we extend the proposed method to two-phase flow in fractured porous media. We perform verification cases and then analyze several cases with a single fracture and a discrete fracture network in two dimensions.

2. Single-phase flow in fractured porous media

2.1. Strong form for single-phase flow in fractured porous media

The fractured porous media is decoupled into two parts, namely, the rock matrix and lower-dimensional fractures. The flow mass balance equations for time-dependent single-phase flow in the matrix and fractures are expressed as:

$$\rho^m SC^m \frac{\partial p^m}{\partial t} + \nabla\cdot(\rho^m \boldsymbol{u}^{\boldsymbol{m}}) = 0 \tag{1}$$

$$d^f \rho^f SC^f \frac{\partial p^f}{\partial t} + \nabla_T\cdot\left(d^f \rho^f \boldsymbol{u}_{\boldsymbol{T}}^{\boldsymbol{f}}\right) = 0 + [\rho^m \boldsymbol{u}^{\boldsymbol{m}}] \tag{2}$$

where p^α is the pore pressure, ρ^α is the fluid density, φ^α is the porosity, and the storage coefficient is $SC^\alpha = \phi^\alpha c_f^\alpha + (1-\phi^\alpha)c_p^\alpha$. c_f^α is the compressibility of the fluid, and c_p^α is the effective compressibility of the solid skeleton. The superscript $\alpha \in \{m, f\}$ denotes the matrix and fracture variables. $d^f$is the fracture aperture. Neglecting the gravity effect, the fluid velocities $\boldsymbol{u}^{\boldsymbol{m}}$ and $\boldsymbol{u}_{\boldsymbol{T}}^{\boldsymbol{f}}$ in the matrix and fracture are described by Darcy's law as follows:

$$\boldsymbol{u}^{\boldsymbol{m}} = -\frac{\boldsymbol{k}^{\boldsymbol{m}}}{\mu^m}\nabla p^m \tag{3}$$

$$\boldsymbol{u}_{\boldsymbol{T}}^{\boldsymbol{f}} = -\frac{\boldsymbol{k}_{\boldsymbol{\tau}}^{\boldsymbol{f}}}{\mu^f}\nabla_T p^f \tag{4}$$

where μ^α is the fluid viscosity, $\boldsymbol{k}^{\boldsymbol{m}}$ is the matrix permeability tensor, and $\boldsymbol{k}_{\boldsymbol{\tau}}^{\boldsymbol{f}}$ is the tangential fracture permeability tensor. $[\rho^m \boldsymbol{u}^m]$ represents the fluid mass exchange between the matrix and fracture. The coupling conditions at the interface between the fractures and matrix are given by (Martin et al., 2005; Antonietti et al., 2019):

$$[\boldsymbol{u}^{\boldsymbol{m}}] = \boldsymbol{u}^{\boldsymbol{m}^+}\cdot\boldsymbol{n}^+ + \boldsymbol{u}^{\boldsymbol{m}^-}\cdot\boldsymbol{n}^- = \alpha_\Gamma\left(p^{m^+} + p^{m^-} - 2p^f\right) \tag{5}$$

$$2\{\boldsymbol{u}^{\boldsymbol{m}}\}\cdot\boldsymbol{n} = \boldsymbol{u}^{\boldsymbol{m}^+}\cdot\boldsymbol{n}^+ - \boldsymbol{u}^{\boldsymbol{m}^-}\cdot\boldsymbol{n}^- = \beta_\Gamma(p^{m^+} - p^{m^-}) \tag{6}$$

where $\beta_\Gamma = \frac{1}{\eta_\Gamma}$, $\eta_\Gamma = \frac{d^f}{2k_n^f}$, $\alpha_\Gamma = \frac{1}{(2\xi-1)}\beta_\Gamma$ and $\boldsymbol{k}_{\boldsymbol{n}}^{\boldsymbol{f}}$ is the normal fracture permeability tensor. The parameter ξ yields different boundary conditions along the interface Martin et al., 2005). Here, we let the $\xi = 0.75$. The notations $[x]$ and $\{x\}$ denote a jump and the average of variable x, respectively (Antonietti et al., 2019; Antonietti et al., 2016). From Eqs. (5) and ((6), we obtain:

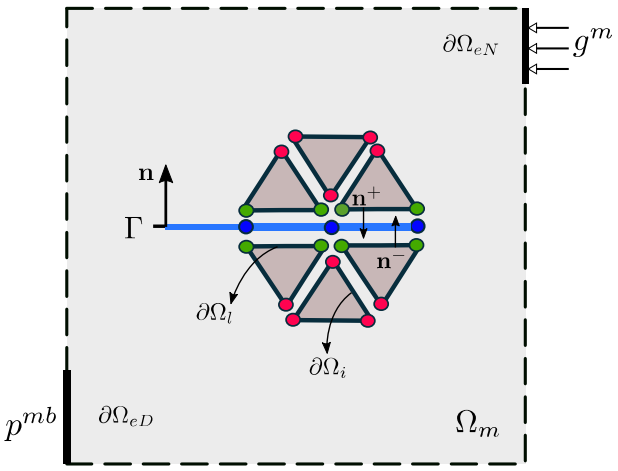

Fig. 1. Illustration of porous media Ω_m containing a fracture Γ with boundary conditions and the corresponding DG elements. $\partial\Omega_{eN}$ and $\partial\Omega_{eD}$ are Neumann and Dirichlet boundaries, $\partial\Omega_i$ are inner mesh boundaries, and $\partial\Omega_l = \Omega_m \cap \Gamma$ is the inner boundary contiguous with fracture.

$$\boldsymbol{u}^{m+}\cdot\boldsymbol{n}^{+} = \frac{1}{2}\left(\vartheta_\Gamma p^{m+} + \varepsilon_\Gamma p^{m-} - 2\alpha_\Gamma p^{f}\right) \tag{7}$$

$$\boldsymbol{u}^{m-}\cdot\boldsymbol{n}^{-} = \frac{1}{2}\left(\varepsilon_\Gamma p^{m+} + \vartheta_\Gamma p^{m-} - 2\alpha_\Gamma p^{f}\right) \tag{8}$$

where $\vartheta_\Gamma = \alpha_\Gamma + \beta_\Gamma$, $\varepsilon_\Gamma = \alpha_\Gamma - \beta_\Gamma$, $\boldsymbol{u}^{m+}$ and $\boldsymbol{u}^{m-}$ denote the flow velocity at the two sides of matrix elements m^+ and m^- neighboring the fracture, and $\boldsymbol{n}$ denotes the unit normal vector oriented from element m^+ to m^-.

2.2. Weak form for single-phase flow in fractured porous media

To develop the weak formulation of the governing equations of fluid flow in fractured porous media, it is necessary to define the boundary conditions of the domain. We consider a two-dimensional domain Ω, containing fracture Γ and porous media $\Omega_m = \Omega/\Gamma$, with the external boundaries $\partial\Omega_e = \partial\Omega_{eN} \cup {}^{\partial}\Omega_{eD}$ and $\partial\Omega_{eN} \cap {}^{\partial}\Omega_{eD} = \varnothing$, as depicted in Fig. 1. $\partial\Omega_{eN}$ and $\partial\Omega_{eD}$ are defined as Neumann and Dirichlet boundary conditions, respectively. The boundaries of the domain are separated into three parts: inner mesh boundaries $\partial\Omega_i$, exterior boundaries $\partial\Omega_e$ and fracture boundaries $\partial\Omega_l = \Omega_m \cap \Gamma$. Let χ be the set of the triangular elements E meshed on the domain Ω_m. ∂E denotes the set of the total edges on boundary. We define the finite element subspace of discontinuous piecewise functions as:

$$Q(\chi) = \left\{V \in L^2(\Omega_m) : V|_E \in P^r(E), \forall E \in \chi\right\} \tag{9}$$

where $P^r(E)$ is the discrete space with the set of polynomials of total degree r. We remark that the approximation of the parameters by discontinuous polynomials of order $r = 2$.

The weak form of the partial differential equations of flow in eq. (1) can be obtained by multiplying the test function for matrix pore pressure $\widetilde{p^m}$ over the one element E in the domain Ω_m. Following Green's first identity and divergence theorem, the weak formulation of the matrix flow equation is expressed as:

$$\int_{\Omega_m} \rho^m SC^m \frac{\partial p^m}{\partial t}\widetilde{p^m}\, d\Omega_m + \int_{\partial E} \lambda^m \nabla p^m \cdot \boldsymbol{n}\widetilde{p^m}\, dS - \int_E \lambda^m \nabla p^m \cdot \nabla\widetilde{p^m}\, dV = 0 \tag{10}$$

where $\lambda^m = -\rho^m \frac{\boldsymbol{k}^m}{\mu^m}$. Here, we weakly enforce the continuity of fluid across the inner mesh boundaries $\partial\Omega_i$. In addition, a symmetric bilinear form and penalty term are added to guarantee the existence of the approximate solution and improve the convergence of the equation (Dolejší and Feistauer, 2015). After applying the average and jump notations introduced above, the second term on the right-hand side in eq. (10) is therefore written as

$$\begin{aligned}
&\int_{\partial E} \lambda^m \nabla p^m \cdot \boldsymbol{n}\widetilde{p^m}\, dS \\
&= \sum_{\partial E \in \partial\Omega_i \cup \partial\Omega_{eD}} \int_{\partial E} \lambda^m \{\nabla p^m\}\left[\widetilde{p^m}\right] + \epsilon\lambda^m\left\{\nabla\widetilde{p^m}\right\}[p^m] + \frac{\delta_p}{h}[p^m]\left[\widetilde{p^m}\right] dS \\
&\quad + \sum_{\partial E \in \partial\Omega_{eN}} \int_{\partial E} \lambda^m \nabla p^m \cdot \boldsymbol{n}\widetilde{p^m} dS \\
&\quad + \sum_{\partial E \in \partial\Omega_l} \int_{\partial E} \left(\rho^{m+}\boldsymbol{u}^{m+}\cdot\boldsymbol{n}^{+}\widetilde{p^{m+}} + \rho^{m+}\boldsymbol{u}^{m-}\cdot\boldsymbol{n}^{-}\widetilde{p^{m-}}\right) dS
\end{aligned} \tag{11}$$

where δ_p is the penalty parameter, h is the mesh size, and ε is the symmetrization parameter. The choice of the parameter ε results in the nonsymmetric interior penalty Galerkin (NIPG) method ($\varepsilon = 1$), the symmetric interior penalty Galerkin (SIPG) method ($\varepsilon = -1$), or the incomplete interior penalty Galerkin (IIPG) method ($\varepsilon = 0$). Here, $\varepsilon = 1$ is chosen. After substituting Eq. (11) into Eq. (10), incorporating the boundary conditions and summing over all the elements in χ, the weak formation of the governing equation is obtained as follows:

$$\begin{aligned}
&\int_{\Omega_m} \rho^m SC^m \frac{\partial p^m}{\partial t}\widetilde{p^m}\, d\Omega_m - \sum_{E\in\chi}\int_E \lambda^m \nabla p^m \cdot \nabla\widetilde{p^m}\, dV \\
&\quad + \sum_{\partial E \in \partial\Omega_i} \int_{\partial E} \lambda^m \{\nabla p^m\}\left[\widetilde{p^m}\right] + \epsilon\lambda^m\left\{\nabla\widetilde{p^m}\right\}[p^m] + \frac{\delta_p}{h}[p^m]\left[\widetilde{p^m}\right] dS \\
&\quad + \sum_{\partial E \in \partial\Omega_{eD}} \int_{\partial E} \lambda^m \nabla p^m \cdot \boldsymbol{n}\widetilde{p^m} + \epsilon\lambda^m \nabla\widetilde{p^m} \cdot \boldsymbol{n}(p^m - p^{mb}) + \frac{\delta_p}{h}(p^m - p^{mb})\widetilde{p^m}\, dS \\
&\quad + \sum_{\partial E \in \partial\Omega_{eN}} \int_{\partial E} \lambda^m g^m \widetilde{p^m}\, dS \\
&\quad + \sum_{\partial E \in \partial\Omega_{el}} \int_{\partial E} \left(\rho^{m+}\boldsymbol{u}^{m+}\cdot\boldsymbol{n}^{+}\widetilde{p^{m+}} + \rho^{m+}\boldsymbol{u}^{m-}\cdot\boldsymbol{n}^{-}\widetilde{p^{m-}}\right) dS = 0
\end{aligned} \tag{12}$$

For simplicity, we assume that the pressure across the fracture nodes is continuous, and the continuous Galerkin (CG) method is employed to discretize the fracture flow equation. We note that the DG approximation for the fracture flow requires additional details without giving an in-depth analysis of the problem (Antonietti et al., 2019). By multiplying the test function $\widetilde{p^f}$ over the fracture domain Γ and applying the divergence theorem and the boundary conditions, the weak form of the fracture flow equation is obtained as follows:

$$\int_{\Gamma}\left(d^f\rho^f SC^f\frac{\partial p^f}{\partial t}\widetilde{p^f}-d^f\lambda^f\nabla_T p^f\cdot\nabla_T\widetilde{p^f}-[\rho^m\boldsymbol{u}^m]\widetilde{p^f}\right)d\Gamma+\int_{\partial\Gamma}d^f\lambda^f\nabla_T p^f\cdot\boldsymbol{n}\widetilde{p^f}\,d\partial\Gamma=0 \tag{13}$$

where $\boldsymbol{u}^{m+}\bullet\boldsymbol{n}^{+}$ and $\boldsymbol{u}^{m-}\bullet\boldsymbol{n}^{-}$ in Eqs. (12) and (13) on two sides of the matrix elements adjacent to fractures are calculated with Eqs. (7) and (8), respectively.

3. Implementation of the numerical methods

Eqs. (12) and (13) are the final weak forms for single-phase flow in fractured porous media. The fluids flow models are implemented and solved with the general-purpose finite element software COMSOL Multiphysics. The built-in COMSOL modules Weak Form PDE and Weak Form Boundary PDE are selected to solve Eqs. (12) and (13), respectively. The discontinuous Galerkin method based on quadratic discontinuous Lagrange shape function is selected to solve the fluid flow problem in porous media with Eq. (12). Fracture flow is implemented using the Weak Form Boundary PDE, and the standard Galerkin method with a quadratic continuous Lagrange shape function is used to discretize Eq. (13).

We use an implicit time step method with a backward differentiation formula (BDF) and an adaptive time step algorithms for time discretization. The pre-established time step method randomly chooses time steps. By default, the first step is 0.1% of the end time, and redundant time step histories can be avoided if the end time is changed. Changing the time step should not, however, considerably change the result if the tolerance is sufficiently tight for automatic time step control. The BDF accuracy of discretization varies from one (that is, backward Euler) to five. A multifrontal massively parallel sparse (MUMPS) direct solver is adopted for the linear system. A fully coupled solver is also selected, and this linear solver is applied to nonlinear problems with Newton's single-step method. In each iteration of Newton's method, we implement constant Newton settings and manually specify a constant damping factor that is used in all iterations.

4. Simulation results

4.1. 2D benchmark case: complex fracture network

In this section, both conducting and blocking fractures are considered with a complex fracture network to illustrate the capability of the proposed model to simulate single-phase flow in fractured porous media. The domain and boundary conditions of the simulation are shown in Fig. 2. The specific coordinates of the fracture positions are taken from reference (Flemisch et al., 2018). The solid and dashed lines in the domain represent fractures with a high permeability of 10^4 and a low permeability of 10^{-4}, respectively. The permeability of the surrounding porous media is **I**. All the fractures are assumed to have the same aperture of 10^{-4} m. The fluid flows from top to bottom in Case (a) and from left to right in Case (b).

Fig. 3 shows the spatial distribution of pressure associated with the pressure profile along the line (0,0.5)-(1.0.9) in Cases (a) and (b) obtained with the DG/CG-FEM method and the solutions of other

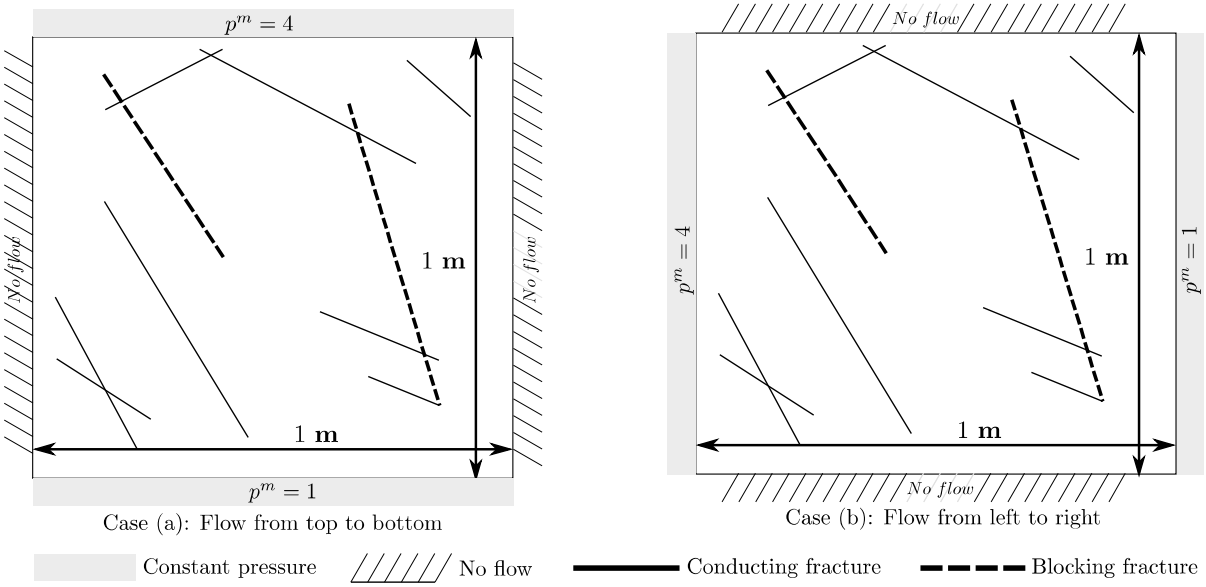

Fig. 2. Domain and boundary conditions for a single flow through porous media with conducting and blocking fractures. The matrix permeability k^m is set to I. The fractures have the same permeability values in the normal and tangential directions. The permeabilities of the conducting and blocking fractures are set to 10^4 and 10^{-4}, respectively. The fluid flows from top to bottom in Case (a) and from left to right in Case (b).

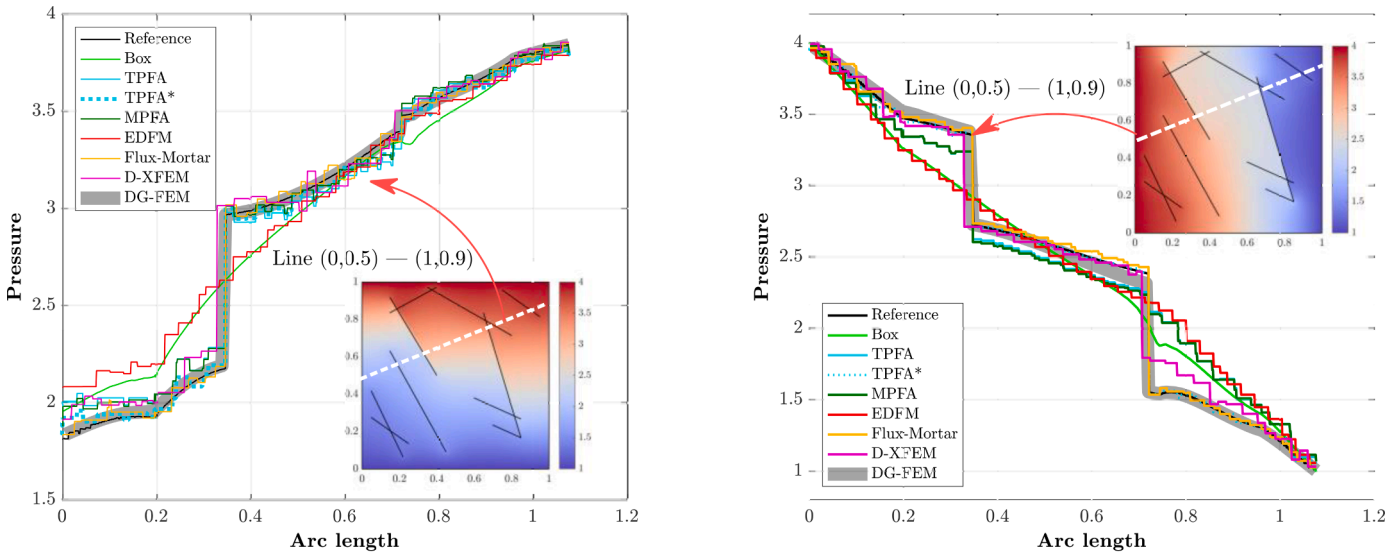

Fig. 3. Pressure values along the observation line and pressure distribution in Cases (a) and (b) obtained with the DG-FEM. The reference solutions are provided in the benchmark study (Flemisch et al., 2018).

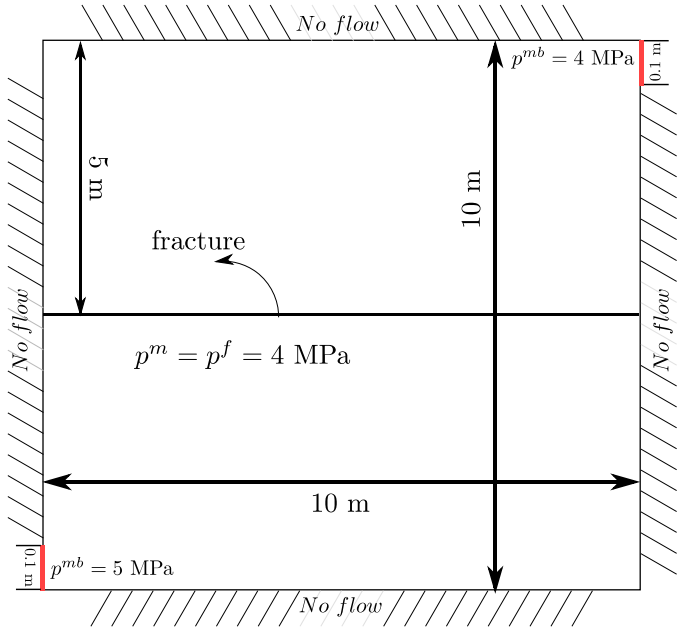

Fig. 4. Description of the geometric configuration and two-dimensional simulation domain with initial conditions and boundary conditions.

numerical methods obtained from the benchmark cases (Flemisch et al., 2018). Here, the reference solutions in Fig. 3 are calculated with mimetic finite differences and fine triangular or quadrilateral element discretization for both matrix and fracture features. The simulated results for a case with a regular fracture network and a realistic case from the benchmark case set (Flemisch et al., 2018) are reported in Appendix A. Apparently, the computed results are in agreement with the solutions of benchmark cases. Moreover, the DG/CG-FEM method is capable of capturing pressure jumps across blocking fractures.

4.2. Time-dependent cases

In this section, we analyze three time-dependent cases with different fracture permeabilities of 10^{-12}, 10^{-17} and 10^{-18} m^2, focusing on investigating the influence of the permeability ratio between the fracture and matrix. In these three cases, the fracture aperture and porosity are 0.01 m and 0.4, and the porosity and permeability of the matrix are 0.1 and 10^{-14} m^2. The fluid density is 1000 kg/m^3, and the viscosity is 10^{-3} Pa . s. The compressibility coefficients of c_f^m and c_p^m are 3.84 $\times$ 10^{-10} Pa^{-1} and 1.00 $\times$ 10^{-8} Pa^{-1}. The geometry and initial conditions of the model are shown in Fig. 4. The simulation domain is 10 m $\times$ 10 m with a single horizontal fracture residing in the middle. The initial pressures in the matrix and fracture are 4MPa. The Dirichlet boundaries of p^{mb} = 4MPa and p^{mb} = 5MPa are imposed on the upper right and the lower left segments with a length of 0.1 m, respectively. For all cases, the simulation time is set to 1 day.

The spatial distributions of pressure with different permeabilities at t = 0.01, 0.10 and 1.00 days are shown in Fig. 5. Fluid is trapped under the fracture and moves horizontally in the case where the permeability of the fracture is lower than that of the neighboring matrix, which gives rise to an obvious decrease in matrix pressure at the two sides of the fracture (Fig. 6). With the increase in fracture permeability, fluid tends to propagate across the fracture and hence results in a relatively continuous pressure at the matrix intersecting with the fracture. The evolution of pressure p^fat the fracture, p^{m-} at the lower matrix grid cell and p^{m+} at the upper matrix grid cell at point p1(5,5) are shown in Fig. 7. The evolution of pressure has similar trends. Pore pressure has different values in the cases with low permeability fractures and maintains continuity for the high fracture permeability.

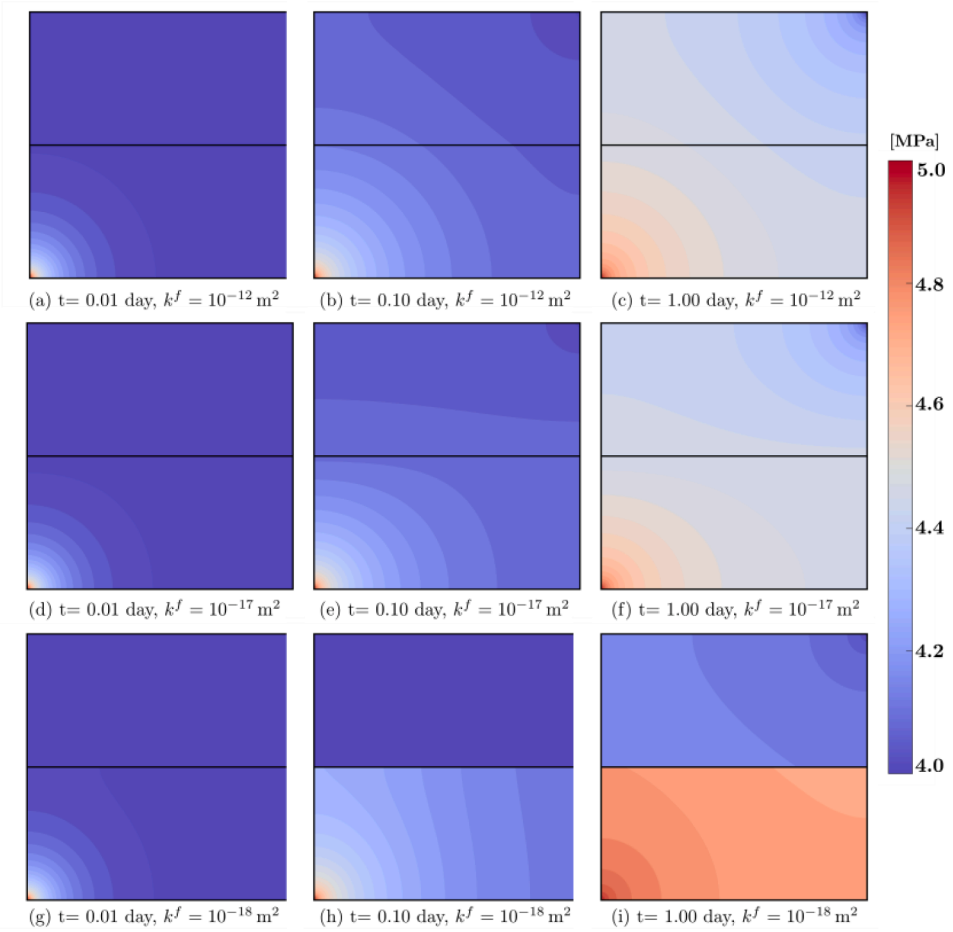

Fig. 5. Pressure distribution at $t = 0.01$, 0.10 and 1.00 days for the cases with low fracture permeabilities of 10^{-12}, 10^{-17} and 10^{-18}m^2. In all three cases, the aperture and porosity of the fracture are 0.01 m and 0.4, respectively. The matrix permeability and porosity are set to 10^{-14} m^2 and 0.1, respectively.

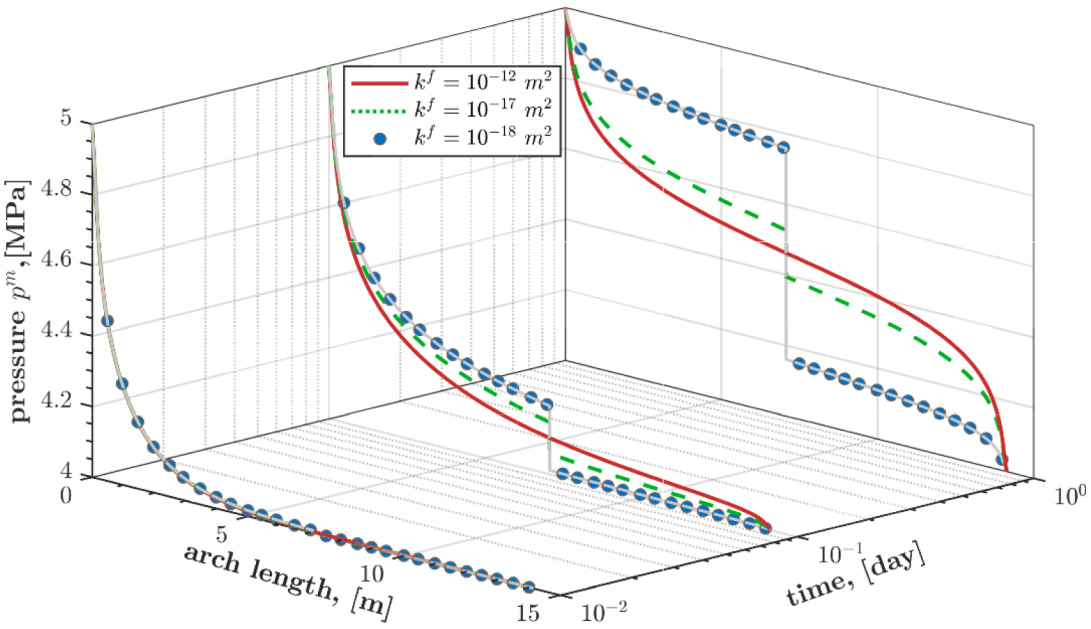

Fig. 6. Pressure profile along the diagonal line from the lower left corner to the upper right corner at $t = 0.01$, 0.10 and 1.00 days for the cases with different fracture permeabilities of 10^{-12}, 10^{-17} and 10^{-18}m^2.

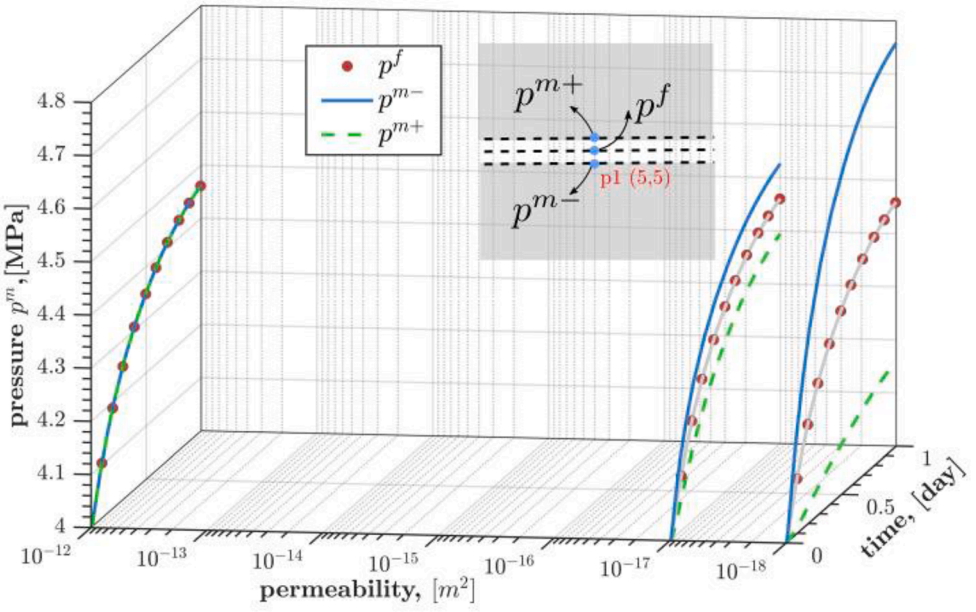

Fig. 7. Temporal evolution of the pressure p^fin the fracture, p^{m-} in the lower matrix grid cell and p^{m+} in the upper matrix grid cell at point p1 with different fracture permeabilities of 10^{-12}, 10^{-17} and 10^{-18}m^2.

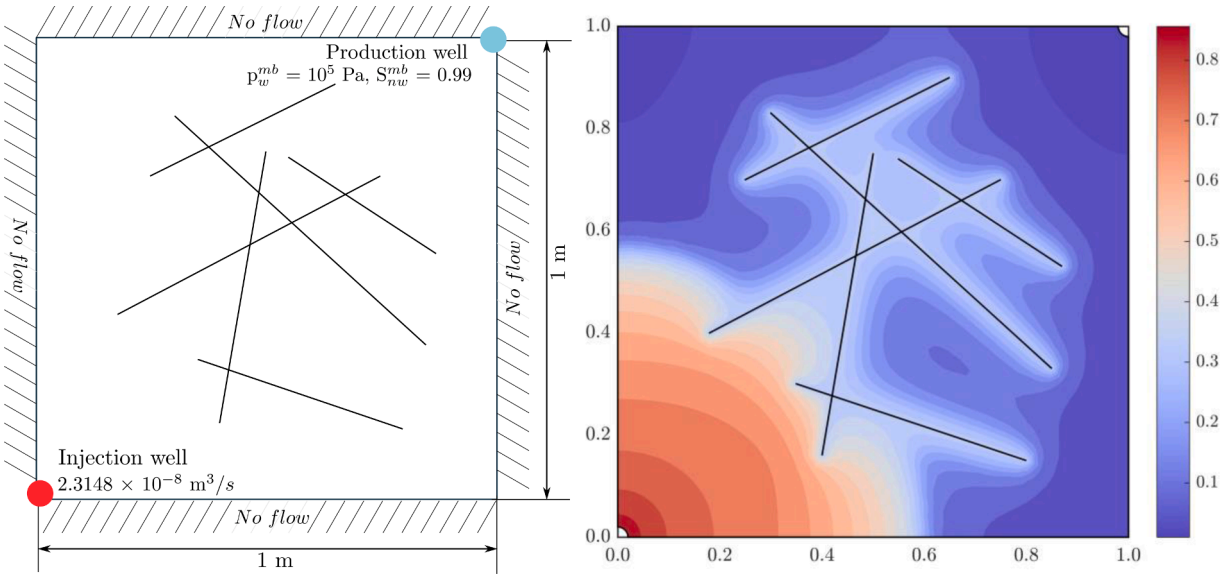

Fig. 8. Geometry and boundary conditions of the model and simulated water saturation. The left figure illustrates the simulation domain and boundary conditions, and the right figure shows the water saturation distribution after 25 days of water injection into a nearly saturated oil reservoir with a multifracture configuration.

Table 1
Material properties of the reservoir and fluids for the two-phase multiple-fracture configuration.

Parameter	Value	Unit
Matrix porosity, φ^m	0.20	[-]
Matrix permeability, k^m	9.87×10^{-16}	[m^2]
Matrix parameters, B^m	1.0	[Pa]
Matrix pore index, ϕ^m	5.0	[-]
Fracture porosity, φ^f	1.0	[-]
Fracture aperture, d^f	1.0×10^{-4}	[m]
Tangential fracture permeability, k_τ^f	8.26×10^{-10}	[m^2]
Normal fracture permeability, k_n^f	8.26×10^{-10}	[m^2]
Matrix parameters, B^f	1.0	[atm]
Fracture pore index, ϕ^f	3.0	[-]
Wetting phase viscosity, μ_w^α	0.8×10^{-3}	[Pa • s]
Wetting density, ρ_w^α	1000	[kg/m^3]
Oil viscosity, μ_{nw}^α	0.45×10^{-3}	[Pa • s]
Oil density, ρ_{nw}^α	600	[kg/m^3]

Table 2
Material properties of the reservoir and fluids for the two-phase multiple-fracture configuration.

	Parameter	Value	Unit
Matrix	Porosity, φ^m	0.20	[-]
	Permeability, k^m	1.0×10^{-14}	[m^2]
	Entry pressure, p_e^m	5.0×10^4	[Pa]
	Pore index, ϕ^m	0.457	[-]
	Parameter, ω^m	0.8	[-]
Fracture	Porosity, φ^f	0.4	[-]
	Aperture, d^f	0.01	[m]
	Tangential permeability, k_τ^f	1.0×10^{-11}	[m^2]
	Normal permeability, k_n^f	1.0×10^{-11}	[m^2]
	Entry pressure, p_e^f	3.0×10^4	[Pa]
	Pore index, ϕ^f	0.457	[-]
	Parameter, ω^f	0.8	[-]
Barrier	Porosity, φ^f	0.1	[-]
	Aperture, d^f	0.01	[m]
	Tangential permeability, k_τ^f	1.0×10^{-17}	[m^2]
	Normal permeability, k_n^f	1.0×10^{-17}	[m^2]
	Entry pressure, p_e^f	8.0×10^4	[Pa]
	Pore index, ϕ^f	0.457	[-]
	Parameter, ω^f	0.8	[-]
Fluid properties	Wetting phase viscosity, μ_w^α	1.0×10^{-3}	[Pa • s]
	Wetting phase density, ρ_w^α	1000	[kg/m^3]
	Compressibility of wetting phase, C_w^α	3.84×10^{-10}	[Pa^{-1}]
	Nonwetting phase viscosity, μ_{nw}^α	9.02×10^{-6}	[Pa • s]
	Nonwetting phase density, ρ_{nw}^α	3.18	[kg/m^3]
	Compressibility of nonwetting phase, C_{nw}^α	7.71×10^{-6}	[Pa^{-1}]

5. Two-phase flow in fractured porous media

Here, we extend the DG/CG method from single-phase flow to compressible two-phase flow in fractured porous media with a mixed-dimensional approach. In this section, we present the strong forms and the corresponding weak forms for two-phase flow in fractured porous media.

The nonwetting phase pressure p_{nw}^α and saturation wetting phase saturation S_w^α are chosen as the primary variables. Without the consideration of gravity, the governing equations for immiscible, compressible two-phase flow in the matrix, together with the generalized Darcy law, are described below (Bjørnarå et al., 2016):

$$\phi^m S_w^m \rho_w^m c_w \frac{\partial p_{nw}^m}{\partial t} + \left(\phi^m \rho_w^m - \phi^m S_w^m \rho_w^m c_w |p_c^m|\right) \frac{\partial S_w^m}{\partial t} + \nabla \cdot \left(-\rho_w^m \frac{\boldsymbol{k}^m k_{rw}^m}{\mu_w} \nabla p_{nw}^m \right) - \nabla \cdot \left(-\rho_w^m \frac{\boldsymbol{k}^m k_{rw}^m}{\mu_w} |p_c^m| \nabla S_w^m \right) = 0 \tag{14}$$

$$\phi^m S_{nw}^m \rho_{nw}^m c_{nw} \frac{\partial p_{nw}^m}{\partial t} - \phi^m \rho_{nw}^m \frac{\partial S_w^m}{\partial t} + \nabla \cdot \left(-\rho_{nw}^m \frac{\boldsymbol{k}^m k_{rnw}^m}{\mu_{nw}} \nabla p_{nw}^m \right) = 0 \tag{15}$$

The governing equations in the fractures are (Ma et al., 2020; Ma et al., 2017):

$$d^f \phi^f S_w^f \rho_w^f c_w \frac{\partial p_{nw}^f}{\partial t} + d^f \left(\phi^f \rho_w^f - \phi^f S_w^f \rho_w^f c_w |p_c^f|\right) \frac{\partial S_w^f}{\partial t} + \nabla_T \cdot \left(-d^f \rho_w^f \frac{\boldsymbol{k}_\tau^f k_{rw}^f}{\mu_w} \nabla p_{nw}^f \right) - \nabla \cdot \left(-d^f \rho_w^f \frac{\boldsymbol{k}_\tau^f k_{rw}^f}{\mu_w} |p_c^f| \nabla S_w^f \right) = \left[\rho_w^m \boldsymbol{u}_w^m\right] \tag{16}$$

$$d^f \phi^f S_{nw}^f \rho_{nw}^f c_{nw} \frac{\partial p_{nw}^f}{\partial t} - d^f \phi^f \rho_{nw}^f \frac{\partial S_{nw}^f}{\partial t} + \nabla_T \cdot \left(-d^f \rho_{nw}^f \frac{\boldsymbol{k}_\tau^f k_{rnw}^f}{\mu_{nw}} \nabla p_{nw}^f \right) = \left[\rho_{nw}^m \boldsymbol{u}_{nw}^m\right] \tag{17}$$

where ρ_β^α is the fluid density, and c_β is the compressibility of fluid. $\beta = nw$ and w represent the nonwetting and wetting phases, respectively.

The capillary pressure p_c^α is a function of the effective saturation s_e^α, which is expressed as $p_c^\alpha = p_{nw}^\alpha - p_w^\alpha = p_e^\alpha (s_e^\alpha)^{-1/\varphi^\alpha}$. The effective saturation s_e^α is equal to $\frac{S_w^\alpha - S_{rw}^\alpha}{1 - S_{rw}^\alpha - S_{rnw}^\alpha}$. $|p_c^\alpha| = \frac{\partial p_{nw}^\alpha}{\partial S_w^\alpha} = \frac{1}{1 - S_{rw}^\alpha - S_{rnw}^\alpha} p_e^\alpha \left(-\frac{1}{\varphi^\alpha}\right) s_e^{\alpha\, -\frac{1}{\varphi^\alpha} - 1}$. $S_{r\beta}^\alpha$ is the residual saturation, p_e^α is the entry pressure, and ϕ^α is the pore size distribution index. The van Genuchten-Mualem model of relative permeability functions is adopted and shown as follows (Pruess et al., 1999):

$$k_{rw}^\alpha = \begin{cases} \sqrt{s_e^\alpha} \left[1 - \left(1 - s_e^{\alpha\, 1/\omega^\alpha}\right)^{\omega^\alpha}\right]^2, & if\ S_w^\alpha < 1 \\ 1, & if\ S_w^\alpha > 1 \end{cases} \tag{18}$$

$$k_{rnw}^\alpha = \begin{cases} 1 - k_{rw}^\alpha, & if\ S_{rnw}^\alpha = 0 \\ \left(1 - s_e^\alpha\right)^2 \left(1 - s_e^{\alpha 2}\right), & if\ S_{rnw}^\alpha > 0 \end{cases} \tag{19}$$

where k_{rw}^α and k_{rnw}^α are the relative permeabilities of the wetting and nonwetting phases, respectively. The flow equations of the matrix and fracture are coupled by linear transmission conditions on the interface described as (Gläser et al., 2019; Brenner et al., 2018; Aghili et al., 2019; Koch et al., 2020):

$$\boldsymbol{u}_\beta^{m+} \cdot \boldsymbol{n}^+ = -\frac{k_n^f k_{r\beta}^f}{\mu_\beta} \left(\frac{p_\beta^{m+} - p_\beta^f}{d^f/2} \right) \tag{20}$$

$$\boldsymbol{u}_\beta^{m-} \cdot \boldsymbol{n}^- = -\frac{k_n^f k_{r\beta}^f}{\mu_\beta} \left(\frac{p_\beta^{m-} - p_\beta^f}{d^f/2} \right) \tag{21}$$

The process of weak form derivation for Eqs. (14)-(17) follows a similar process to that of Eqs. (1) and (2), with different numbers of unknown variables and equations. Similarly, interior penalty discontinuous Galerkin (IPDG) discretization for two-phase flow equations in the matrix is expressed as:

$$
\begin{aligned}
&\int_{\Omega_{\mathrm{m}}}\left[\phi^m S_w^m \rho_w^m c_w \frac{\partial p_{nw}^m}{\partial t}+\left(\phi^m \rho_w^m-\phi^m S_w^m \rho_w^m c_w|p_c^m|\right)\frac{\partial S_w^m}{\partial t}\right]\widetilde{S_w^m}\,d\Omega_{\mathrm{m}}\\
&+\sum_{E\in\chi}\int_E(\lambda_w^m|p_c^m|\nabla S_w^m-\lambda_w^m\nabla p_{nw}^m)\cdot\nabla\widetilde{S_w^m}\;dV\\
&+\sum_{\partial E\in\partial\Omega_i}\int_{\partial E}-(\lambda_w^m|p_c^m|)\{\nabla S_w^m\}\left[\widetilde{S_w^m}\right]+\epsilon(\lambda_w^m|p_c^m|)\{\nabla\widetilde{S_w^m}\}[S_w^m]+\frac{\delta_p}{h}[S_w^m]\left[\widetilde{S_w^m}\right]\,dS\\
&+\sum_{\partial E\in\partial\Omega_i}\int_{\partial E}\lambda_w^m\{\nabla p_{nw}^m\}\left[\widetilde{S_w^m}\right]+\epsilon\lambda_w^m\{\nabla\widetilde{S_w^m}\}[p_{nw}^m]+\frac{\delta_p}{h}[p_{nw}^m]\left[\widetilde{S_w^m}\right]\,dS\\
&+\sum_{\partial E\in\partial\Omega_{eD}}\int_{\partial E}-(\lambda_w^m|p_c^m|)\nabla S_w^m\cdot\boldsymbol{n}\,\widetilde{S_w^m}\;dS\\
&+\sum_{\partial E\in\partial\Omega_{eD}}\int_{\partial E}\epsilon(\lambda_w^m|p_c^m|)\nabla\widetilde{S_w^m}\cdot\boldsymbol{n}\,(S_w^m-S_w^{mb})+\frac{\delta_p}{h}(S_w^m-S_w^{mb})\widetilde{S_w}\,dS\\
&+\sum_{\partial E\in\partial\Omega_{eD}}\int_{\partial E}\lambda_w^m\nabla p_{nw}^m\cdot\boldsymbol{n}\,\widetilde{S_w^m}\;dS\\
&+\sum_{\partial E\in\partial\Omega_{eD}}\int_{\partial E}\epsilon\lambda_w^m\nabla\widetilde{S_w}\cdot\boldsymbol{n}(\,p_{nw}^m-p_{nw}^{mb})+\frac{\delta_p}{h}(\,p_{nw}^m-p_{nw}^{mb})\widetilde{S_w}\,dS\\
&+\sum_{\partial E\in\partial\Omega_{eN}}\int_{\partial E}\lambda_w^m g_w^m\widetilde{S_w}dS\\
&+\sum_{\partial E\in\partial\Omega_l}\int_{\partial E}\rho_{nw}^{m+}\boldsymbol{u_w^{m+}}\cdot\boldsymbol{n}^+\widetilde{S_w^{m+}}+\rho_{nw}^{m-}\boldsymbol{u_w^{m-}}\cdot\boldsymbol{n}^-\widetilde{S_w^{m-}}\,dS=0
\end{aligned}
\tag{22}
$$

$$
\begin{aligned}
&\int_{\Omega_{\mathrm{m}}}\left(\phi^m S_{nw}^m\rho_{nw}^m c_{nw}\frac{\partial p_{nw}^m}{\partial t}-\phi^m\rho_{nw}^m\frac{\partial S_{nw}^m}{\partial t}\right)\widetilde{p_{nw}^m}d\Omega_{\mathrm{m}}-\sum_{E\in\chi}\int_E\lambda_{nw}^m\nabla p_{nw}^m\cdot\nabla\widetilde{p_{nw}^m}\;dV\\
&+\sum_{\partial E\in\partial\Omega_i}\int_{\partial E}\lambda_{nw}^m\{\nabla p_{nw}^m\}\left[\widetilde{p_{nw}^m}\right]+\epsilon\lambda_{nw}^m\{\nabla\widetilde{p_{nw}^m}\}[p_{nw}^m]+\frac{\delta_p}{h}[p_{nw}^m]\left[\widetilde{p_{nw}^m}\right]dS\\
&+\sum_{\partial E\in\partial\Omega_{eD}}\int_{\partial E}\lambda_{nw}^m\nabla p_{nw}^m\cdot\boldsymbol{n}\,\widetilde{p_{nw}^m}\;dS\\
&+\sum_{\partial E\in\partial\Omega_{eD}}\int_{\partial E}\epsilon\lambda_{nw}^m\nabla\widetilde{p_{nw}^m}\cdot\boldsymbol{n}\,(p_{nw}^m-p_{nw}^{mb})+\lambda_{nw}^m\nabla\widetilde{p_{nw}^m}\cdot\boldsymbol{n}\,(p_{nw}^m-p_{nw}^{mb})\;dS\\
&+\sum_{\partial E\in\partial\Omega_{eN}}\int_{\partial E}\lambda_{nw}^m\,g_{nw}^m\widetilde{p_{nw}^m}dS\\
&+\sum_{\partial E\in\partial\Omega_l}\int_{\partial E}\rho_{nw}^{m+}\boldsymbol{u_{nw}^+}\cdot\boldsymbol{n}^+\widetilde{p_{nw}^{m+}}+\rho_{nw}^{m-}\boldsymbol{u_{nw}^-}\cdot\boldsymbol{n}^-\widetilde{p_{nw}^{m-}}\,dS=0
\end{aligned}
\tag{23}
$$

The weak forms of the fracture flow equations are described as follows:

$$
\begin{aligned}
&\int_\Gamma\left[d^f\phi^f S_{nw}^f\rho_{nw}^f c_w\frac{\partial p_{nw}^f}{\partial t}+d^f\left(\phi^f\rho_w^f-\phi^f S_w^f\rho_w^f c_w|p_c^f|\right)\frac{\partial S_w^f}{\partial t}-\left[\rho_w^m\boldsymbol{u_w^m}\right]\right]\widetilde{S_w^f}d\Gamma\\
&+\int_\Gamma d^f\lambda_w^f|p_c^f|\nabla_T S_w^f\cdot\nabla_T\widetilde{S_w^f}d\Gamma-\int_\Gamma d^f\lambda_w^f\nabla_T p_{nw}^f\cdot\nabla_T\widetilde{S_w^f}d\Gamma-\int_{\partial\Gamma}d^f\lambda_w^f|p_c^f|\nabla_T S_w^f\cdot\boldsymbol{n}\,\widetilde{S_w^f}d\partial\Gamma\\
&+\int_{\partial\Gamma}d^f\lambda_w^f\nabla p_{nw}^f\cdot\boldsymbol{n}\widetilde{S_w^f}d\partial\Gamma=0
\end{aligned}
\tag{24}
$$

$$
\begin{aligned}
&\int_\Gamma\left[d^f\phi^f S_{nw}^f\rho_{nw}^f c_{nw}\frac{\partial p_{nw}^f}{\partial t}-d^f\phi^f\rho_{nw}^f\frac{\partial S_{nw}^f}{\partial t}-\left[\rho_{nw}^m\boldsymbol{u_{nw}^m}\right]\right]\widetilde{p_{nw}^f}d\Gamma\\
&-\int_\Gamma d^f\lambda_{nw}^f\nabla_T p_{nw}^f\cdot\nabla_T\widetilde{p_{nw}^f}\;d\Gamma+\int_{\partial\Gamma}d^f\lambda_{nw}^f\nabla_T p_{nw}^f\cdot\boldsymbol{n}\;\widetilde{p_{nw}^f}\;d\partial\Gamma=0
\end{aligned}
\tag{25}
$$

where $\widetilde{S_\beta^\alpha}$ and $\widetilde{p_\beta^\alpha}$ are the test functions for the saturation and pressure. $S_\beta^{\alpha b}$ and $p_\beta^{\alpha b}$ denote the saturation and pressure on the boundaries. The terms $[\rho_\beta^m\boldsymbol{u_\beta^m}]$ in Eqs. (22)-(25) are obtained from Eqs. (20) and (21), g_β^m is the flow flux on the boundaries.

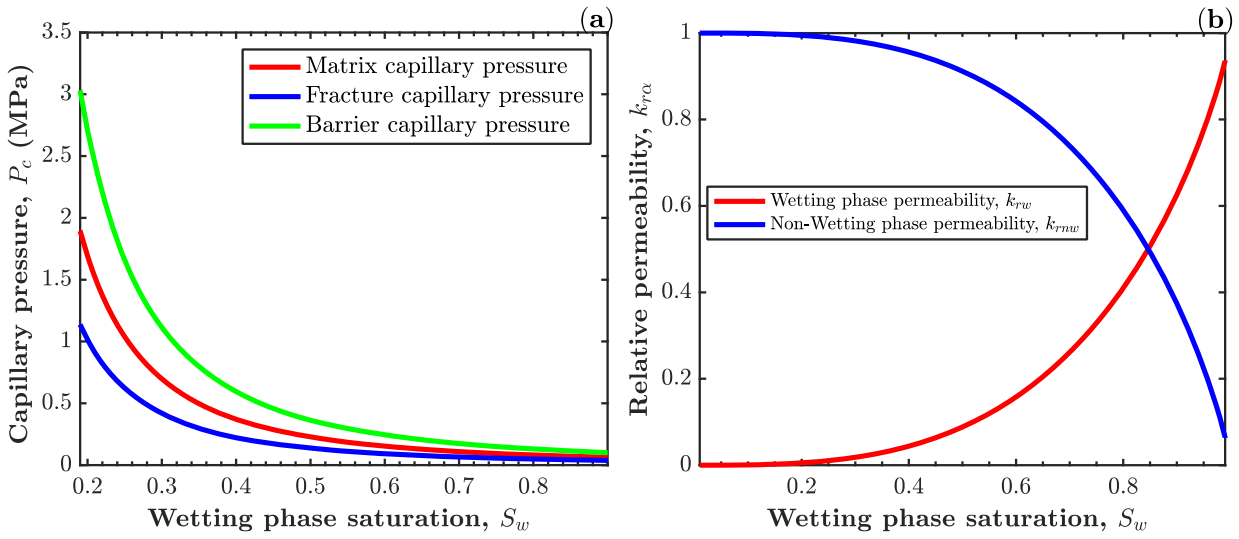

Fig. 9. (a) Brooks and Corey capillary pressure and (b) van Genuchten-Mualem model for relative permeability.

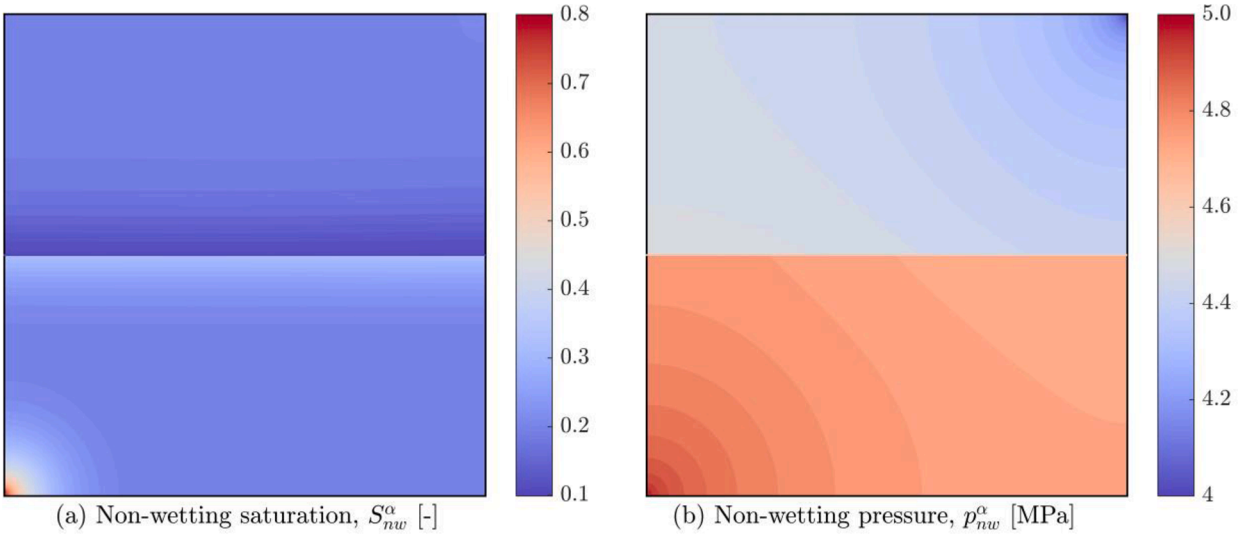

Fig. 10. Distributions of (a) nonwetting saturation S^{α}_{nw} and (b) nonwetting pressure p^{α}_{nw} at $t = 1$ day for the case with a barrier.

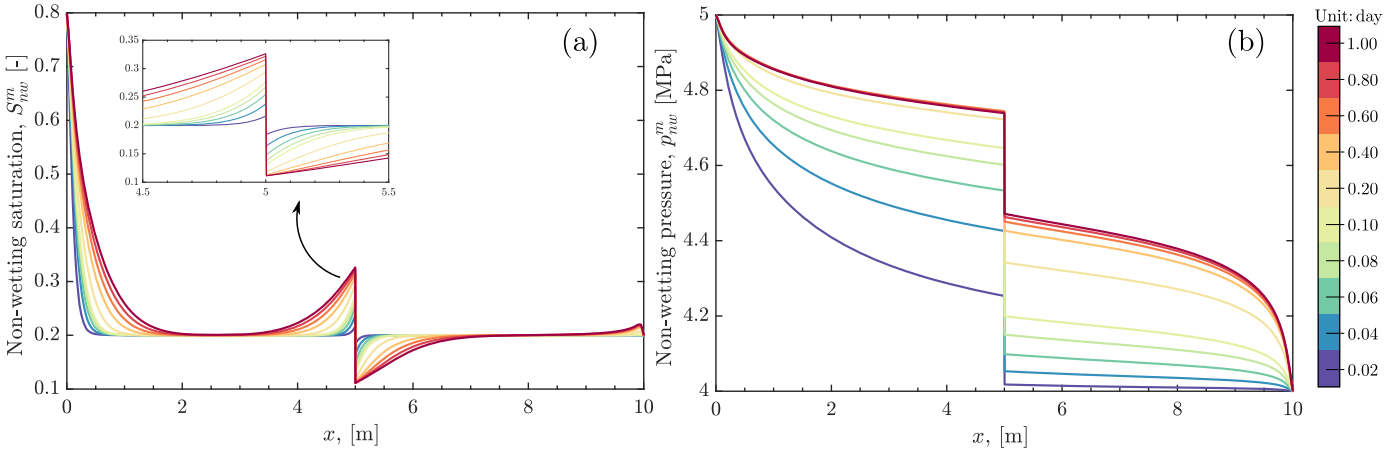

Fig. 11. Nonwetting saturation S^{m}_{nw} and pressure p^{m}_{nw} along the diagonal line (0.0,0.0) - (10.0,10.0) at $t = 0.02$, 0.04, 0.06, 0.08, 0.10, 0.20, 0.40, 0.60, 0.80 and 1.00 days in the case with a barrier.

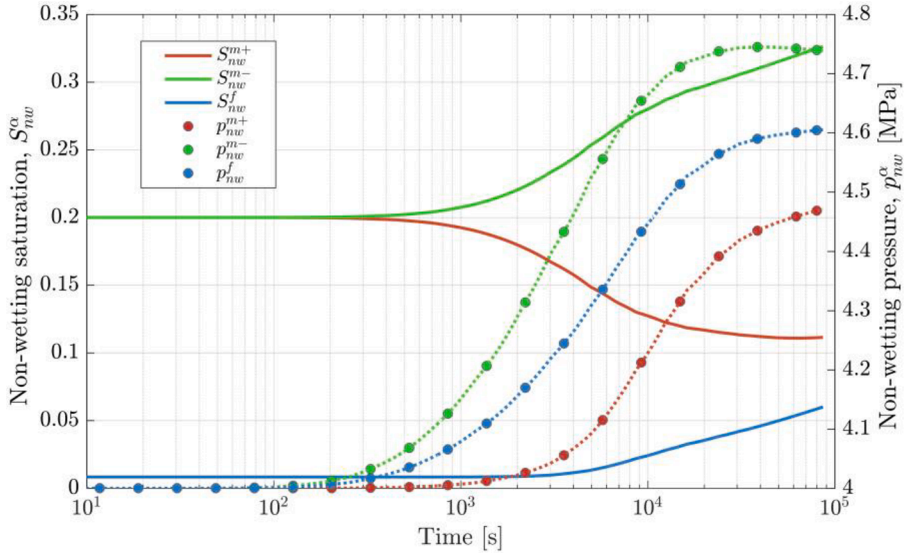

Fig. 12. Evolution of nonwetting saturation and nonwetting pressure at point (5,5) in the matrix-fracture interface.

6. Verification

In this section, we analyze a numerical case to verify the accuracy of the proposed method for two-phase flow in discrete fractured porous media. In this case, we consider a nearly saturated oil reservoir of 1 m × 1 m with complex fractures. The initial conditions that $p^{mb}_{w} = 10^5$ Pa and $S^{mb}_{nw} = 0.99$ are set. The final simulation time is set to 25 days. The geometry and boundary conditions are illustrated in Fig. 8. The input parameters of the reservoir and fluid properties are given in Table 1. The capillary pressure p^{α}_{c} is calculated by $-B^{\alpha}\ln S^{\alpha}_{w}$. The relative permeabilities of oil and water are calculated by $k^{m}_{rnw} = (1 - S^{\alpha}_{w})^{\omega^{\alpha}}$ and $k^{m}_{rw} = (S^{\alpha}_{w})^{\omega^{\alpha}}$, respectively.

Fig. 8 shows the computed water saturation distribution after 25 days of injection. The water is likely to flow through the fracture as a result of the high fracture permeability. Good agreement is achieved between the current simulated result and that of the reference model (Ma et al., 2020; Monteagudo and Firoozabadi, 2004).

7. Applications

7.1. Case 1: single fracture

In this section, we describe two cases with high and low permeable fractures. The simulation geometry described in Fig. 4 is adopted. The initial nonwetting pressure of the matrix and fracture are 4 MPa, and the initial wetting saturation in the matrix is 0.8. To ensure initial flow balance between the matrix and fracture system, $p^{m0}_{w} = p^{f0}_{w}$ is assumed. Hence, the initial wetting saturation in the fracture can be calculated by $S^{f0}_{w} = S^{f}_{wr} + (1 - S^{f}_{wr} - S^{f}_{nwr})\left(\frac{p^{f}_{e}}{p^{m}_{e}}\right)^{\varphi^{f}} (S^{m0}_{e})^{\frac{\varphi^{f}}{\varphi^{m}}}$. $p^{mb}_{nw} = 5$ MPa and $S^{mb}_{w} = 0.2$ are set on the lower left boundary. The values of pressure and saturation on the upper right boundary are equal to the initial conditions. The present model does not consider the extended pressure conditions at the interface (Reichenberger et al., 2006). Thus, the entry pressure of the matrix and fracture need to be appropriately assigned in both cases with high and low permeability fractures to ensure saturation within

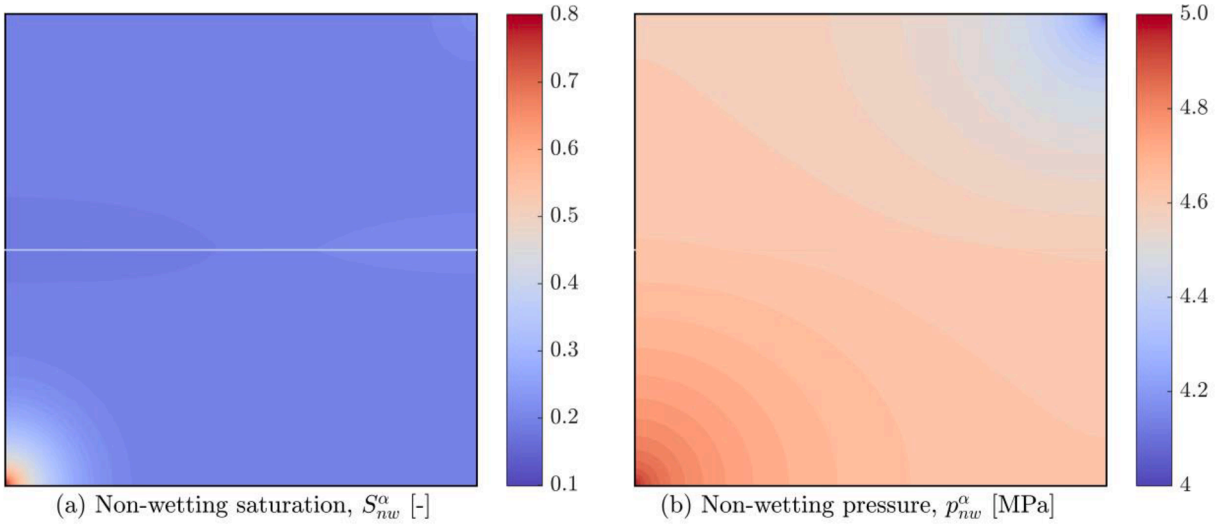

Fig. 13. Distribution of (a) nonwetting saturation S^{α}_{nw} and (b) nonwetting pressure p^{α}_{nw} at $t = 1$ day for the case with fracture.

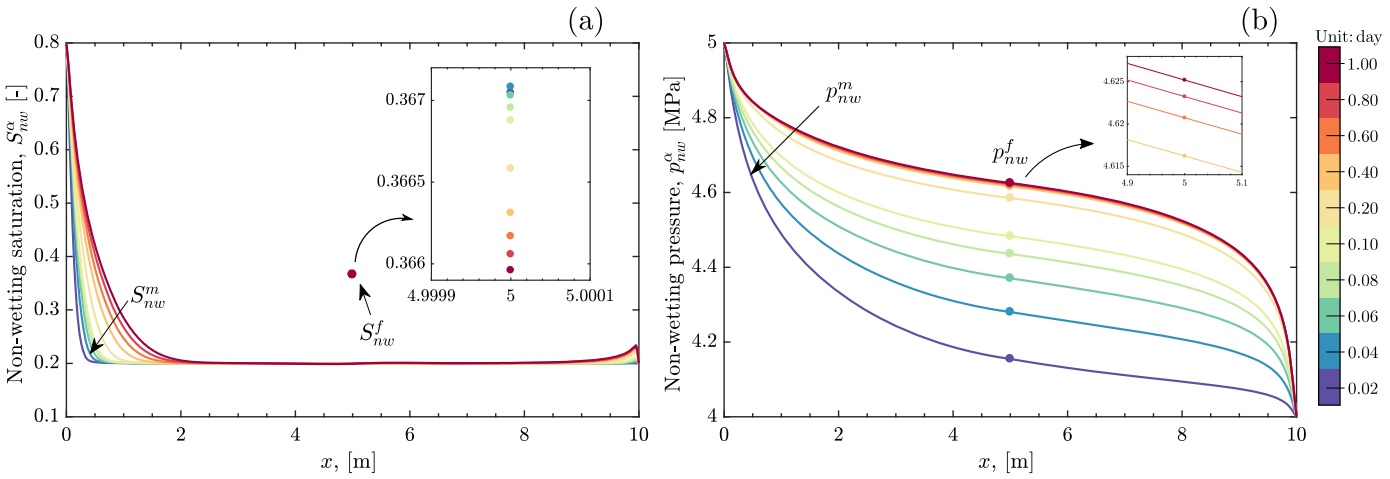

Fig. 14. Nonwetting saturation S^{m}_{nw} and pressure p^{m}_{nw} along the diagonal line (0.0,0.0) - (10.0,10.0) and S^{f}_{nw} and p^{f}_{nw} at the point (5,5) (scatters) at $t = 0.02$, 0.04, 0.06, 0.08, 0.10, 0.20, 0.40, 0.60, 0.80 and 1.00 days in the case with fracture.

reasonable limits. Here, the wetting phase and nonwetting phase refer to water and hydrogen, respectively. The fluid properties are obtained from NIST (Lemmon, 1998). The entry pressures and other parameters are listed in Table 2. The Brooks and Corey capillary pressure curves for the matrix, fracture and barrier are illustrated in Fig. 9(a). The relative permeability curves of water and hydrogen for the matrix and fracture are shown in Fig. 9(b).

The nonwetting saturation S^{α}_{nw} and nonwetting pressure p^{α}_{nw} distributions at $t = 1$ day are shown in Fig. 10. The nonwetting saturation S^{m}_{nw} and pressure p^{m}_{nw} along the diagonal line (0.0,0.0) - (10.0,10.0) at $t =$ 0.02, 0.04, 0.06, 0.08, 0.10, 0.20, 0.40, 0.60, 0.80 and 1.00 days in the case with a barrier are shown in Fig. 11. The evolution of S^{α}_{nw} and p^{α}_{nw} at the point on the interface is illustrated in Fig. 12. Due to the low permeability of the barrier, the fluids barely flow across the barrier, which results in an obvious pressure jump between the neighboring two sides of the fracture. Additionally, the fluid is trapped near the fracture as a result of high entry pressure associated with the corresponding capillary pressure of the barrier. The discontinuity in saturation can be explained by the fact that the nonwetting phase pressure propagates ahead of the saturation front (Gläser et al., 2017), which causes the corresponding mass transfer between the fracture and the neighboring matrix.

Fig. 13 shows the nonwetting saturation S^{m}_{nw} and nonwetting pressure p^{m}_{nw} distributions at $t = 1$ day in the case with a highly permeable fracture dividing in the domain. Fig. 14 illustrates the nonwetting saturation S^{m}_{nw} and pressure p^{m}_{nw} along the diagonal line and S^{f}_{nw} and p^{f}_{nw} at the point (5,5) at specific time points in the case of conducting fracture. The saturation and pressure decrease from the inlet to the outer boundary. After 1 day of injection, the hydrogen front propagated more than 3 m away from the lower-left corner. After the pressure reaches the fracture and flows across the fracture, as a consequence of the highly permeable fracture, a negligible pressure and saturation difference is evident between the two sides of the fracture. Due to the initial flow equilibrium condition at the interface, the high permeability of the fracture gives rise to an approximately equivalent pressure in the two domains that results in an obvious saturation difference between the fracture and matrix because of the different capillary pressures of the matrix and fracture.

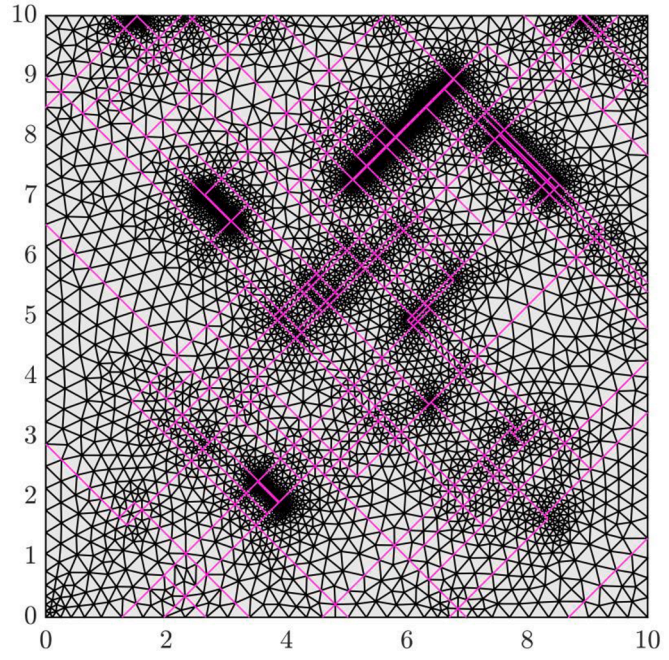

Fig. 15. Spatial discretization of the simulation domain with a discrete fracture network. Refined tetrahedral meshes are generated in areas with multiple fractures or short fractures. Magenta lines indicate the low-dimension fractures.

7.2. *Case 2: discrete fracture network*

In this section, we study a simulation case with a discrete fracture network, which is created by the open source tool DFNE (Alghalandis, 2017). Two sets of orthogonal fractures are oriented at angles of 45° and 135° in a square domain with a length of 10 m. The initial and boundary condition settings are the same as those in the cases with a single fracture in Section 7.1 We explore two cases with fractures and barriers, respectively. Fig. 15 shows the spatial discretization of the model domain. The model domain is discretized into more than 21,000 tetrahedral elements, 2800 edge elements and 280 vertex elements. Grid refinement is automatically performed in the areas with multiple fractures or short fractures.

The distributions of the nonwetting saturation S^{m}_{nw} and pressure p^{m}_{nw} in the case with low permeable fracture networks and the S^{m}_{nw} and p^{m}_{nw} distributions based on height expression after 1 day of gas injection are shown in Fig. 16. The pressure propagates into the reservoirs while the

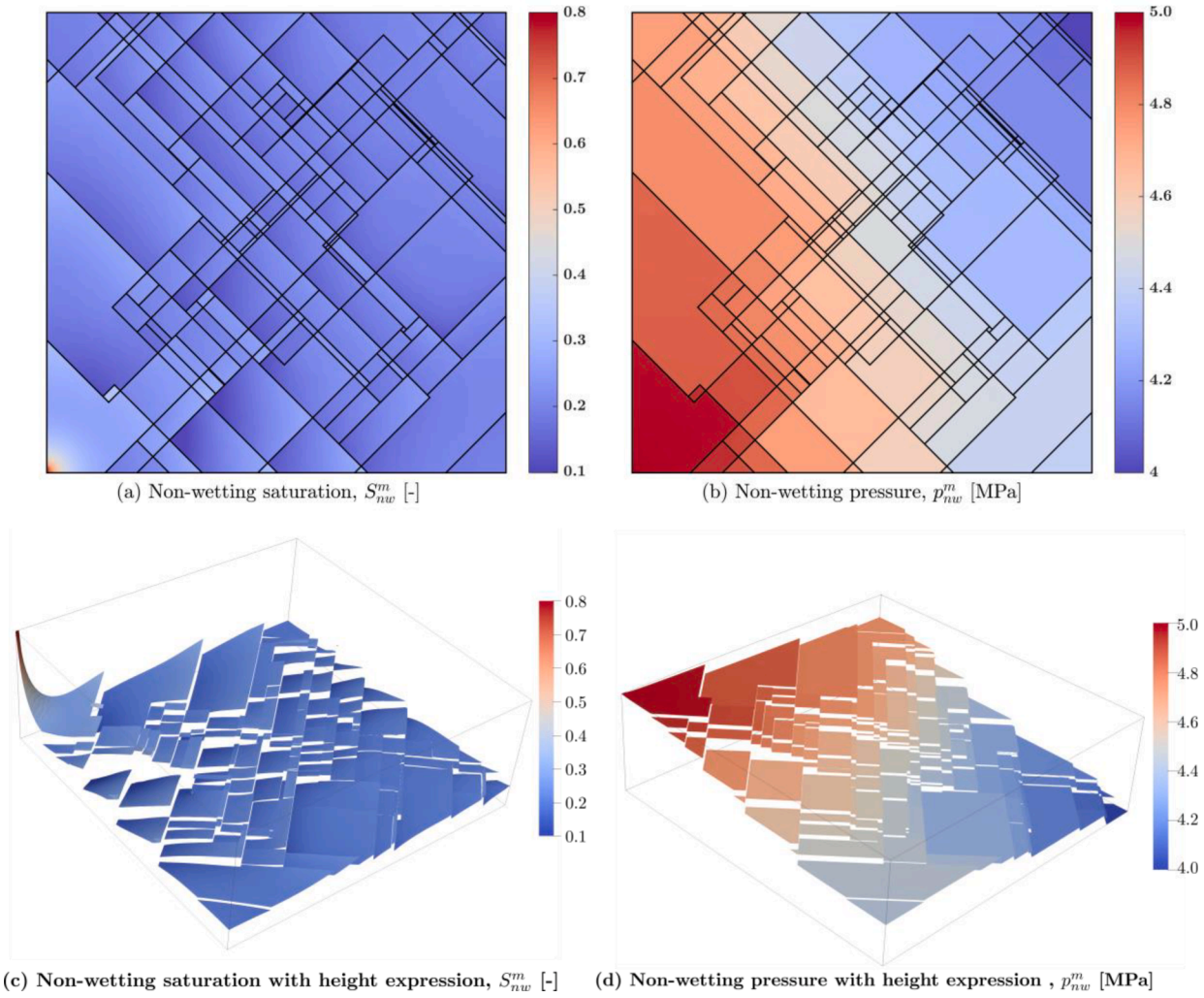

Fig. 16. Distributions of (a) nonwetting saturation S_{nw}^m and (b) pressure p_{nw}^m in the case with low permeable fracture networks. (c) S_{nw}^m and (d) p_{nw}^m distributions based on height expression after 1 day of gas injection.

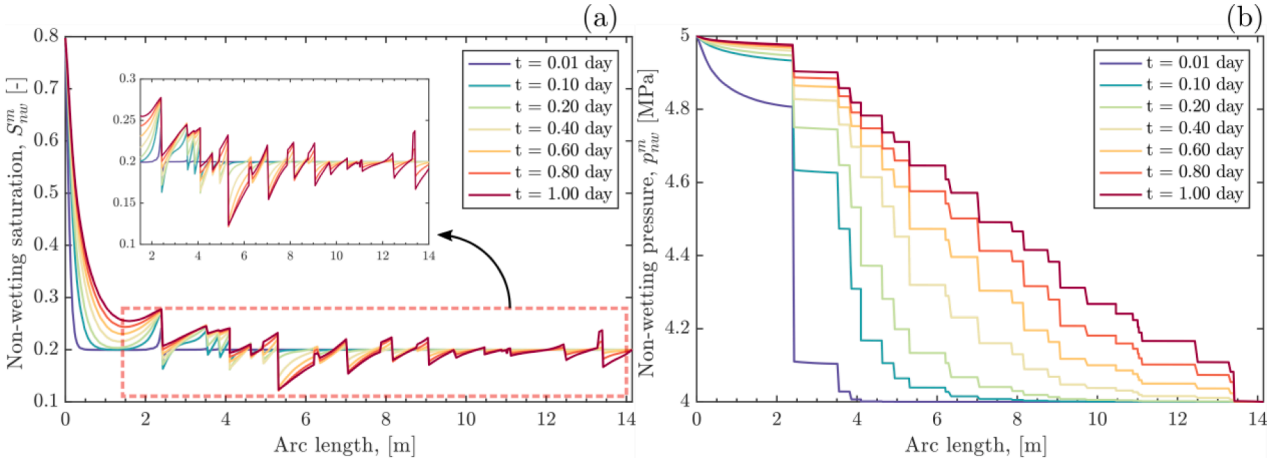

Fig. 17. Nonwetting saturation S_{nw}^m and pressure p_{nw}^m along the diagonal line at t = 0.01, 0.10, 0.20, 0.40, 0.60, 0.80 and 1.00 days in the case with a highly permeable fracture network.

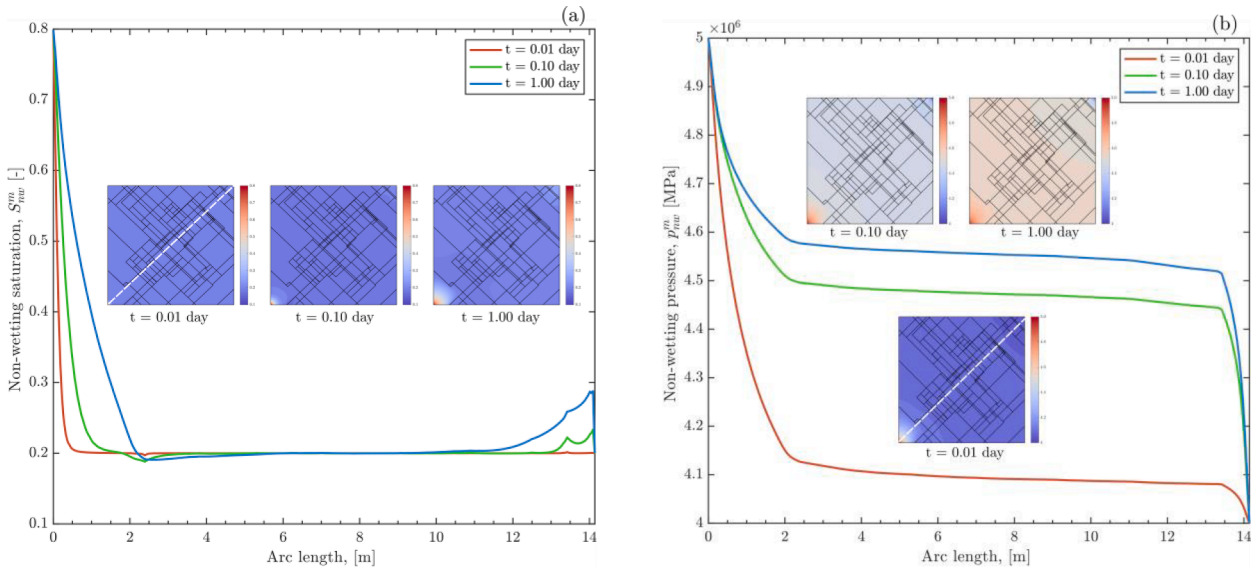

Fig. 18. S_{nw}^m and p_{nw}^m distributions and profiles along the diagonal line at $t = 0.01$, 0.10, and 1.00 days in the case with a highly permeable fracture network.

gas is trapped around the injection boundary. The pressure decreases stepwise, and saturation decreases with a local wave type pattern along the diagonal line (Fig. 17). Pressure and saturation between the two sides of fractures appear discontinuous in the case with blocking fractures and continuous in the case with conducting fractures (Figs. 17 and 18).

8. Summary and conclusion

In this paper, we presented a discontinuous and continuous Galerkin (DG/CG) approximation for modeling single-phase and two-phase flow in porous media with a mixed-dimensional approach, in which fractures were described as a (d-1)-dimensional interface embedded in a D-dimensional domain based on the linear transmission conditions at the matrix–fracture interfaces.

The proposed model was first verified for single-phase flow in a complex fracture network involving both conducting and blocking fractures. Our simulation results are in good agreement with the reference benchmark solutions, which demonstrates the feasibility and accuracy of the DG/CG method. Then, time-dependent single-phase flow cases were studied. The simulation results illustrate the ability of the presented DG method to capture the discontinuities and continuities with barriers and highly conductive fractures in compressible single-phase flow.

Subsequently, we presented DG approximations for immiscible and compressible two-phase flow in fractured porous media with consideration of the capillary pressure effect. Water injection in discrete-fractured media saturated with oil were analyzed to verify and demonstrate the performance and accuracy of the proposed method in the application of two-phase flow in fractured porous media. Then, the verified model was applied to two-phase problems involving highly conductive and low-permeability fractures. These results illustrate that the DG method captures the continuous pressure, jump in pressure and saturation of the matrix adjacent to the fractures.

Author statement

Tianran Ma: Conceptualization, Methodology, Software, Investigation, Writing - Original draft

Keni Zhang: Supervision, Methodology, Writing-Review & Editing

Weijun Shen: Supervision, Methodology, Validation, Writing-Review & Editing

Chaobin Guo: Investigation, Conceptualization, Writing-Review & Editing

Hao Xu: Conceptualization, Methodology, Visualization, Writing-Review & Editing

Declaration of Competing Interest

The authors declare no conflict of interest.

Acknowledgments

This study was supported by the National Natural Science Foundation of China (Nos. 42002255 and 41902310), Jiangsu Province Natural Science Foundation (No. BK20180636), and the Chinese Geological Survey (No. DD20201165). Special thanks to the anonymous reviewers for their valuable comments.ik

Appendix

Case A.1: Regular fracture network

Case A.2: A realistic case

Fig. A1

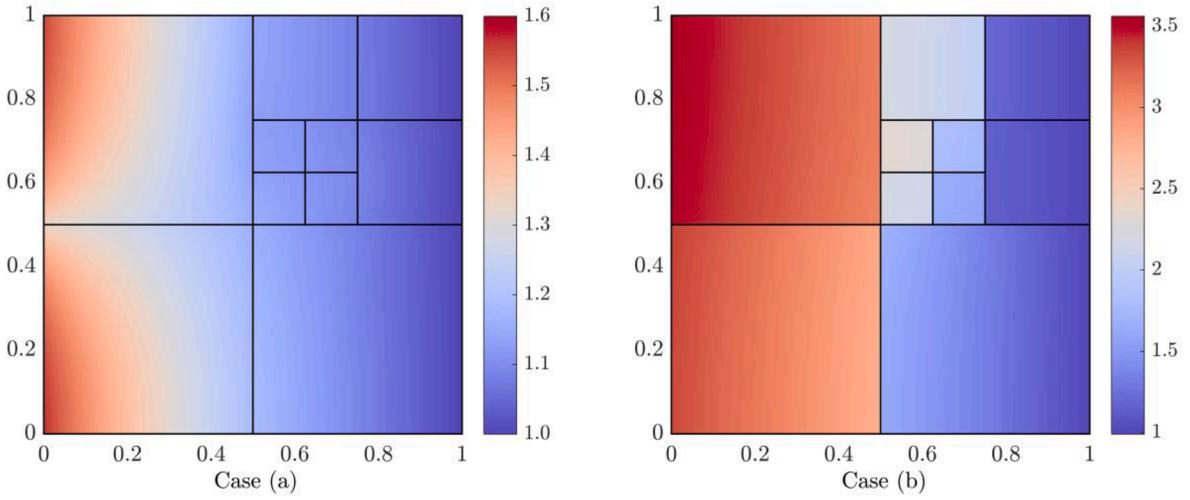

Fig. A1. Distribution of the pore pressure in case a with conductive fractures and case b with blocking fractures. In both cases, the matrix permeability and fracture apertures are set to $k_m = \mathrm{I}$ and 10^{-4}, respectively. The permeability of the fracture is the same in the normal and tangential directions. In cases a and b, the fracture permeabilities are 10^4 and 10^{-4}, respectively. The initial conditions, boundary conditions, and other information are provided in reference (Flemisch et al., 2018).

Fig. A2

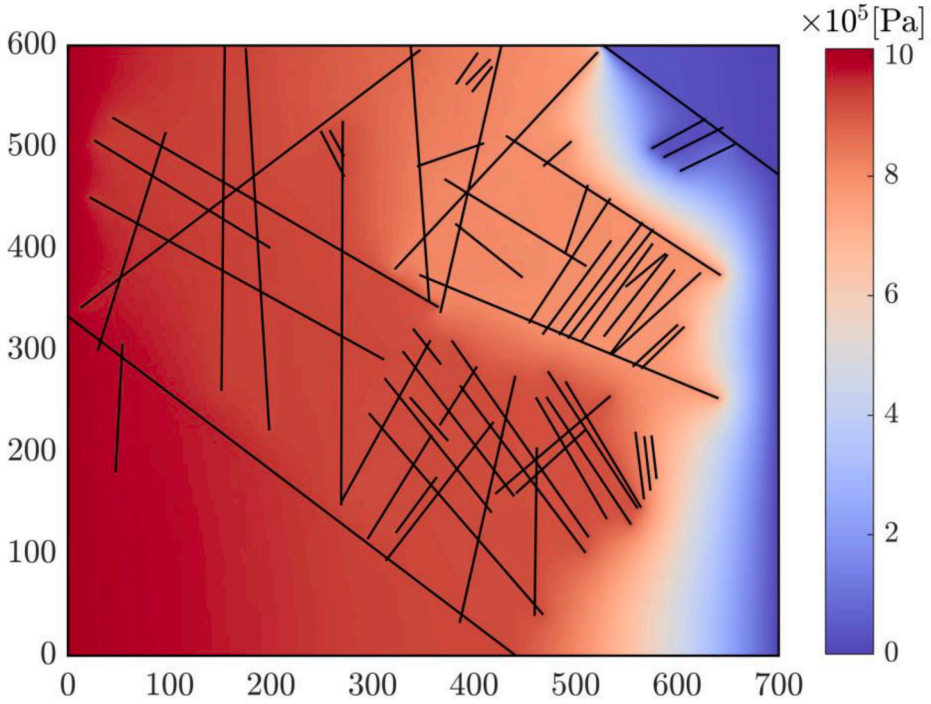

Fig. A2. Distribution of the pore pressure of the benchmark case with real discrete fractures. The size of the domain is 700 m × 600 m. The permeability of the matrix and fracture are 10^{-14} and 10^{-10} m^2, respectively. The initial pressure of the entire domain is 0 Pa for the benchmark case. The pressures on the left and right boundaries are set to 1,013,250 Pa and 0 Pa, respectively. The top and bottom boundaries are no-flow boundaries.

Fig. A3

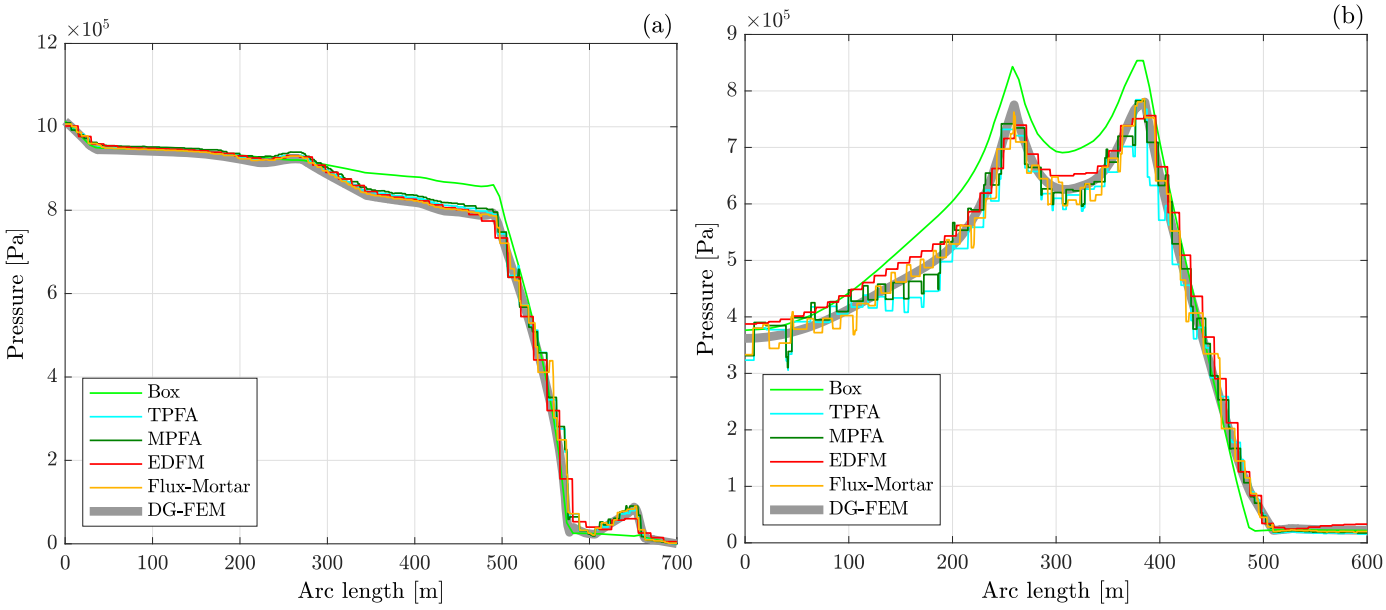

Fig. A3. Profiles of pressure along the lines (a) $y = 500$ m and (b) $x = 625$ m. The gray lines are the simulated results of the DG-FEM, and other solutions are provided in the reference (Flemisch et al., 2018).

References

Aghili, J., Brenner, K., Hennicker, J., Masson, R., Trenty, L., 2019. Two-phase Discrete Fracture Matrix models with linear and nonlinear transmission conditions. GEM-Int. J. Geomath. 10, 1.

Alghalandis, Y.F., 2017. ADFNE: open source software for discrete fracture network engineering, two and three dimensional applications. Comput. Geosci. 102, 1–11.

Antonietti, P.F., Formaggia, L., Scotti, A., Verani, M., Verzott, N., 2016. Mimetic finite difference approximation of flows in fractured porous media. ESAIM: Math. Modell. Numer. Anal. 50, 809–832.

Antonietti, P.F., Facciola, C., Russo, A., Verani, M., 2019. Discontinuous Galerkin approximation of flows in fractured porous media on polytopic grids. SIAM J. Sci. Comput. 41. A109-A38.

Antonietti P.F., C. Facciolà, M. Verani. Unified analysis of discontinuous Galerkin approximations of flows in fractured porous media on polygonal and polyhedral grids. (2020).

Arbogast, T., Juntunen, M., Pool, J., Wheeler, M.F., 2013. A discontinuous Galerkin method for two-phase flow in a porous medium enforcing H (div) velocityand continuous capillary pressure. Comput. Geosci. 17, 1055–1078.

Bastian, P., 2014. A fully-coupled discontinuous Galerkin method for two-phase flow in porous media with discontinuous capillary pressure. Comput. Geosci. 18, 779–796.

Bjørnarå, T.I., Nordbotten, J.M., Park, J., 2016. Vertically integrated models for coupled two-phase flow and geomechanics in porous media. Water Resour. Res. 52, 1398–1417.

Brenner, K., Hennicker, J., Masson, R., Samier, P., 2018. Hybrid-dimensional modelling of two-phase flow through fractured porous media with enhanced matrix fracture transmission conditions. J. Comput. Phys. 357, 100–124.

Cappanera, L., Rivière, B., 2019. Discontinuous Galerkin method for solving the black-oil problem in porous media. Numer. Methods Partial Differ. Equ. 35, 761–789.

D'Angelo, C., Scotti, A., 2012. A mixed finite element method for Darcy flow in fractured porous media with non-matching grids. ESAIM Math. Model. Num. Anal.-Modélisation Mathématique et Analyse Numérique 46, 465–489.

Dolejší, V., Feistauer, M., 2015. Discontinuous galerkin method. Anal. Appl. Compress. Flow Springer Series Comput. Math. 48.

Epshteyn, Y., Rivière, B., 2007. Fully implicit discontinuous finite element methods for two-phase flow. Appl. Num. Math. 57, 383–401.

Ern, A., Mozolevski, I., 2012. Discontinuous Galerkin method for two-component liquid–gas porous media flows. Comput. Geosci. 16, 677–690.

Flemisch, B., Berre, I., Boon, W., Fumagalli, A., Schwenck, N., Scotti, A., et al., 2018. Benchmarks for single-phase flow in fractured porous media. Adv. Water Resour. 111, 239–258.

Fumagalli, A., Scotti, A., 2013. A numerical method for two-phase flow in fractured porous media with non-matching grids. Adv. Water Resour. 62, 454–464.

Gläser, D., Helmig, R., Flemisch, B., 2017. H Class. A discrete fracture model for two-phase flow in fractured porous media. Adv. Water Resour. 110, 335–348. https://doi.org/10.1016/j.advwatres.2017.10.031.

Gläser, D., Flemisch, B., Helmig, R., Class, H., 2019. A hybrid-dimensional discrete fracture model for non-isothermal two-phase flow in fractured porous media. GEM-Int. J. Geomath. 10, 5.

Hoteit, H., Firoozabadi, A., 2008. An efficient numerical model for incompressible two-phase flow in fractured media. Adv. Water Resour. 31, 891–905.

Jamei, M., Ghafouri, H., 2016. An efficient discontinuous Galerkin method for two-phase flow modeling by conservative velocity projection. Int. J. Num. Method Heat Fluid Flow.

Jiang, J., Yang, J., 2018. Coupled fluid flow and geomechanics modeling of stress-sensitive production behavior in fractured shale gas reservoirs. Int. J. Rock Mech. Min. Sci. 101, 1–12. https://doi.org/10.1016/j.ijrmms.2017.11.003.

Jiang, J., Younis, R.M., 2017. An Improved Projection-based Embedded Discrete Fracture Model (pEDFM) for Multiphase Flow in Fractured Reservoirs. Adv. Water Resour. 109.

Jin, L., Zoback, M., 2017. Fully coupled nonlinear fluid flow and poroelasticity in arbitrarily fractured porous media: a hybrid-dimensional computational model. J. Geophys. Res. 122, 7626–7658.

Kadeethum, T., Nick, H., Lee, S., Ballarin, F., 2020. Flow in porous media with low dimensional fractures by employing enriched Galerkin method. Adv. Water Resour. 142, 103620.

Karimi-Fard, M., Durlofsky, L.J., Aziz, K., 2004. An efficient discrete-fracture model applicable for general-purpose reservoir simulators. SPE J. 9, 227–236.

Khoei, A., Hosseini, N., Mohammadnejad, T., 2016. Numerical modeling of two-phase fluid flow in deformable fractured porous media using the extended finite element method and an equivalent continuum model. Adv. Water Resour. 94, 510–528.

Klieber, W., Riviere, B., 2006. Adaptive simulations of two-phase flow by discontinuous Galerkin methods. Comput. Methods Appl. Mech. Eng. 196, 404–419.

Koch, T., Gläser, D., Weishaupt, K., Ackermann, S., Beck, M., Becker, B., et al., 2020. DuMux 3–an open-source simulator for solving flow and transport problems in porous media with a focus on model coupling. Comput. Math. Appl.

Lemmon, E.W., 1998. Thermophysical properties of fluid systems. NIST Chem. WebBook.

Lepillier, B., Daniilidis, A., Doonechaly Gholizadeh, N., Bruna, P.-O., Kummerow, J., Bruhn, D., 2019. A fracture flow permeability and stress dependency simulation applied to multi-reservoirs, multi-production scenarios analysis. Geothermal Energy 7, 24. https://doi.org/10.1186/s40517-019-0141-8.

Li, L., Lee, S.H., 2008. Efficient field-scale simulation of black oil in a naturally fractured reservoir through discrete fracture networks and homogenized media. SPE Reservoir Eval. Eng. 11, 750–758.

Ma, T., Rutqvist, J., Oldenburg, C.M., Liu, W., Chen, J., 2017. Fully coupled two-phase flow and poromechanics modeling of coalbed methane recovery: impact of geomechanics on production rate. J. Nat. Gas Sci. Eng. 45, 474–486.

Ma, T., Xu, H., Guo, C., Fu, X., Liu, W., Yang, R., 2020. A Discrete Fracture Modeling Approach for Analysis of Coalbed Methane and Water Flow in a Fractured Coal Reservoir. Geofluids 2020, 8845348. https://doi.org/10.1155/2020/8845348.

March, R., Doster, F., Geiger, S., 2018a. Assessment of CO2 Storage Potential in Naturally Fractured Reservoirs With Dual-Porosity Models. Water Resour. Res. 54, 1650–1668. https://doi.org/10.1002/2017wr022159.

March, R., Doster, F., Geiger, S., 2018b. Assessment of CO2 Storage Potential in Naturally Fractured Reservoirs With Dual-Porosity Models. Water Resour. Res. 54, 1650–1668.
Martin, V., Jaffré, J., Roberts, J.E., 2005. Modeling fractures and barriers as interfaces for flow in porous media. SIAM J. Sci. Comput. 26, 1667–1691.
Monteagudo, J., Firoozabadi, A., 2004. Control-volume method for numerical simulation of two-phase immiscible flow in two-and three-dimensional discrete-fractured media. Water Resour. Res. 40.
Oda, M., 1985. Permeability tensor for discontinuous rock masses. Geotechnique 35, 483–495.
Pruess, K., Oldenburg, C.M., Moridis, G., 1999. TOUGH2 User's Guide Version 2. Lawrence Berkeley National Lab.(LBNL), Berkeley, CA (United States).
Reichenberger, V., Jakobs, H., Bastian, P., Helmig, R., 2006. A mixed-dimensional finite volume method for two-phase flow in fractured porous media. Adv. Water Resour. 29, 1020–1036.
Ren, F., Ma, G., Wang, Y., Fan, L., Zhu, H., 2017. Two-phase flow pipe network method for simulation of CO2 sequestration in fractured saline aquifers. Int. J. Rock Mech. Min. Sci. 98, 39–53. https://doi.org/10.1016/j.ijrmms.2017.07.010.
Riviere, B., Yang, X., 2017. A DG Method for the Simulation of CO2 Storage in Saline Aquifer. Adv. Math. Sci. 205.
Saiers, J.E., Barth, E., 2012. Potential Contaminant Pathways from Hydraulically Fractured Shale Aquifers. Groundwater 50, 826–828. https://doi.org/10.1111/j.1745-6584.2012.00990.x.
Salimzadeh, S., Nick, H.M., 2019. A coupled model for reactive flow through deformable fractures in Enhanced Geothermal Systems. Geothermics 81, 88–100. https://doi.org/10.1016/j.geothermics.2019.04.010.
Ţene, M., Bosma, S.B., Al Kobaisi, M.S., Hajibeygi, H., 2017. Projection-based embedded discrete fracture model (pEDFM). Adv. Water Resour. 105, 205–216.
Warren, J., Root, P.J., 1963. The behavior of naturally fractured reservoirs. Soc. Petrol. Eng. J. 3, 245–255.
Wu, Y.-S., Liu, H., Bodvarsson, G., 2004. A triple-continuum approach for modeling flow and transport processes in fractured rock. J. Contam. Hydrol. 73, 145–179.
Yang, R., Ma, T., Xu, H., Liu, W., Hu, Y., Sang, S., 2019. A model of fully coupled two-phase flow and coal deformation under dynamic diffusion for coalbed methane extraction. J. Nat. Gas Sci. Eng. 72, 103010.
Zidane, A., Firoozabadi, A., 2017. Fracture-cross-flow equilibrium in compositional two-phase reservoir simulation. SPE J. 22, 950–970.
Zidane, A., Firoozabadi, A., 2020. Higher-order simulation of two-phase compositional flow in 3D with non-planar fractures. J. Comput. Phys. 402, 108896.